Article

TRANSPARENT PROCESS

THE EMBO JOURNAL

Nanoscale segregation of actin nucleation and elongation factors determines dendritic spine protrusion

Anaël Chazeau[1,2,†], Amine Mehidi[1,2], Deepak Nair[1,2], Jérémie J Gautier[3], Cécile Leduc[4,5], Ingrid Chamma[1,2], Frieda Kage[6], Adel Kechkar[1,2], Olivier Thoumine[1,2], Klemens Rottner[6,7], Daniel Choquet[1,2], Alexis Gautreau[3], Jean-Baptiste Sibarita[1,2] & Grégory Giannone[1,2,*]

Abstract

Actin dynamics drive morphological remodeling of neuronal dendritic spines and changes in synaptic transmission. Yet, the spatiotemporal coordination of actin regulators in spines is unknown. Using single protein tracking and super-resolution imaging, we revealed the nanoscale organization and dynamics of branched F-actin regulators in spines. Branched F-actin nucleation occurs at the PSD vicinity, while elongation occurs at the tip of finger-like protrusions. This spatial segregation differs from lamellipodia where both branched F-actin nucleation and elongation occur at protrusion tips. The PSD is a persistent confinement zone for IRSp53 and the WAVE complex, an activator of the Arp2/3 complex. In contrast, filament elongators like VASP and formin-like protein-2 move outwards from the PSD with protrusion tips. Accordingly, Arp2/3 complexes associated with F-actin are immobile and surround the PSD. Arp2/3 and Rac1 GTPase converge to the PSD, respectively, by cytosolic and free-diffusion on the membrane. Enhanced Rac1 activation and Shank3 over-expression, both associated with spine enlargement, induce delocalization of the WAVE complex from the PSD. Thus, the specific localization of branched F-actin regulators in spines might be reorganized during spine morphological remodeling often associated with synaptic plasticity.

Keywords branched F-actin regulators; dendritic spine; postsynaptic density; single protein tracking; super-resolution microscopy
Subject Category Neuroscience
DOI 10.15252/embj.201488837 | Received 28 April 2014 | Revised 13 August 2014 | Accepted 25 August 2014 | Published online 7 October 2014
The EMBO Journal (2014) 33: 2745–2764

See also: **PP Boyl & W Witke** (December 2014)

Introduction

In the brain, most excitatory postsynapses are located in small membrane extensions called dendritic spines. The morphological remodeling of spines is coupled to changes in synaptic transmission. This constitutes a structural plasticity often associated with learning and memory (Cingolani & Goda, 2008). Indeed, long-term potentiation and depression are correlated with spine head enlargement and shrinkage, respectively (Matsuzaki *et al*, 2004; Okamoto *et al*, 2004; Zhou *et al*, 2004). Spines are genuine motile structures both in neuronal cultures and in intact brains (Fischer *et al*, 1998; Dunaevsky *et al*, 1999; Lendvai *et al*, 2000; Berning *et al*, 2012). Those movements and morphological remodeling rely on the assembly, stabilization and disassembly of F-actin networks concentrated in spines (Okamoto *et al*, 2004; Cingolani & Goda, 2008; Honkura *et al*, 2008; Bosch *et al*, 2014).

Essential F-actin regulators are located in spines (Hotulainen & Hoogenraad, 2010). Among them, regulators of branched F-actin networks critically control spinogenesis, spine morphology, synaptic transmission, synaptic plasticity and cognitive functions. These include not only the Rho-family GTPase Rac1 (Tashiro & Yuste, 2004; Xie *et al*, 2007; Haditsch *et al*, 2009; Fortin *et al*, 2010), the membrane-associated I-BAR protein IRSp53 (Bockmann *et al*, 2002; Choi *et al*, 2005), but also their downstream targets, the WAVE complex (Kim *et al*, 2006; Soderling *et al*, 2007), a nucleation promoting factor, leading to Arp2/3 complex activation and nucleation of branched F-actin networks (Hotulainen *et al*, 2009; Korobova & Svitkina, 2010; Kim *et al*, 2013). Control of F-actin length in spines is then ensured by elongation factors such as VASP and formins (Hotulainen *et al*, 2009; Lin *et al*, 2010) and by capping proteins (Korobova & Svitkina, 2010; Fan *et al*, 2011), while F-actin turnover depends on severing proteins such as ADF/cofilin

1 Interdisciplinary Institute for Neuroscience, University Bordeaux, UMR 5297, Bordeaux, France
2 CNRS, Interdisciplinary Institute for Neuroscience, UMR 5297, Bordeaux, France
3 CNRS UPR3082, Laboratoire d'Enzymologie et Biochimie Structurales, Gif-sur-Yvette Cedex, France
4 University Bordeaux, LP2N, Talence, France
5 CNRS & Institut d'Optique, LP2N, Talence, France
6 Division of Molecular Cell Biology, Zoological Institute, Technical University Braunschweig, Braunschweig, Germany
7 Helmholtz Centre for Infection Research, Braunschweig, Germany
*Corresponding author. Tel: +33 5 57 57 57 44; E-mail: gregory.giannone@u-bordeaux2.fr
†Present address: Cell Biology, Faculty of Science, Utrecht University, Utrecht, The Netherlands

(Gu *et al*, 2010; Rust *et al*, 2010; Bosch *et al*, 2014). Consistent with a critical role of branched F-actin regulators during synaptic transmission, neurological disorders associated with abnormal spine morphologies are triggered by genetic deregulation of proteins, such as Shank3 and FMRP, which directly interact with subunits of the WAVE and Arp2/3 complexes (Schenck *et al*, 2003; Durand *et al*, 2012; De Rubeis *et al*, 2013; Han *et al*, 2013).

Those F-actin regulators also control the formation of membrane protrusions such as the lamellipodium (Hotulainen & Hoogenraad, 2010), suggesting that assembly and disassembly of branched F-actin networks in spines use similar mechanisms. The spatiotemporal coordination of F-actin regulators in the lamellipodium determines the polarity, architecture and movements of branched F-actin networks (Pollard & Cooper, 2009). Nucleation events driven by the WAVE complex and elongation events driven by VASP and formin-like proteins-2 (FMNL2) are all localized at protrusion tips (Rottner *et al*, 1999; Miki *et al*, 2000; Breitsprecher *et al*, 2011; Block *et al*, 2012). Consequently, Arp2/3 complexes and actin monomers are incorporated into branched F-actin networks growing against the lamellipodium tip, while ADF/cofilin associates with the entire network inducing F-actin severing (Iwasa & Mullins, 2007; Lai *et al*, 2008). This organization leads to a concerted retrograde flow of branched F-actin networks (Pollard & Cooper, 2009). However, within micron-size spines, conventional fluorescent microscopy cannot achieve the spatial resolution required to unveil the mechanism of branched F-actin network formation.

Recent studies used super-resolution light microscopy to describe the nanoscale organization of post-synaptic scaffolds and neurotransmitter receptors (Dani *et al*, 2010; Fukata *et al*, 2013; MacGillavry *et al*, 2013; Maglione & Sigrist, 2013; Nair *et al*, 2013). In this study, we used single protein tracking (SPT) and super-resolution microscopy (Betzig *et al*, 2006; Manley *et al*, 2008; Van de Linde *et al*, 2011; Rossier *et al*, 2012) to decipher the nanoscale organization and dynamics of branched F-actin regulators within mature spines. Here, we asked whether distinct regulators of branched F-actin are compartmentalized in dendritic spines and how their spatiotemporal coordination determines the formation and movements of branched F-actin networks. We found that the PSD is the convergence zone where proteins involved in branched F-actin nucleation meet with highest probability. In contrast, proteins triggering F-actin elongation are concentrated at the tips of transient membrane protrusions moving away from the PSD. We also demonstrated that this specific organization of F-actin regulators could be modified in concert with changes in spine morphology. Thus, the nanoscale reorganization of branched F-actin regulators could be the basis of spine morphological remodeling driven by F-actin polymerization during structural plasticity and neurological disorders.

Results

F-actin and the Arp2/3 complex are not exhibiting concerted rearward flow in spines

In classical protrusive structures, including lamellipodia of motile cells and neuronal growth cones, F-actin movements are highly polarized rearward, fast and driven by F-actin growth against the tip of membrane protrusions (Ponti *et al*, 2004; Medeiros *et al*, 2006; Giannone *et al*, 2007; Lai *et al*, 2008). Strong evidence that F-actin rearward movements in spines are powered by the same mechanism is lacking. Previous studies reported that the velocity of the bulk rearward F-actin flow is slow (Honkura *et al*, 2008; Frost *et al*, 2010). In addition, tracking of individual F-actin revealed both slow rearward and forward movements (Tatavarty *et al*, 2009, 2012) and faster rearward movements (Frost *et al*, 2010). Therefore, the exact organization, polarity and dynamics of F-actin networks in spines are still unclear. The Arp2/3 complex is involved in dendritic spine formation, suggesting that the continual nucleation of branched F-actin networks maintains the globular shape of the spine head (Hotulainen *et al*, 2009; Korobova & Svitkina, 2010; Lippi *et al*, 2011; Kim *et al*, 2013). In order to specifically determine the dynamics of branched F-actin networks, we compared F-actin and Arp2/3 movements in mature spines and growth cones of primary rat hippocampal neurons. We used actin and the ArpC5A subunit of the Arp2/3 complex fused to a photoswitchable mEOS2 fluorescent protein. We performed single protein tracking of Arp2/3 and actin after mEOS2 photoactivation (sptPALM) (Manley *et al*, 2008). To measure only the slow mEOS2 movements, we used low-frequency and long-exposure acquisition (2 Hz, 250 ms) as previously described (Tatavarty *et al*, 2009; Frost *et al*, 2010). We analyzed trajectories longer than 4 s and measured start-to-end velocities (resolution > 6 nm s^{-1}, see Materials and Methods). In the growth cone, actin-mEOS2 and mEOS2-ArpC5A movements were fast and highly polarized rearward (Fig 1A, B and D; actin 52 nm s^{-1}, ArpC5A 55 nm s^{-1}). This fast flow of F-actin was drastically decreased by Cytochalasin D treatment (CD) (Fig 1D; actin 21 nm s^{-1}). These results confirmed that F-actin movements in growth cones are largely powered by actin polymerization against the tip of membrane protrusions. In contrast, actin-mEOS2 and mEOS2-ArpC5A movements in spines were slow and not polarized rearwards (Fig 1A, B and D; actin 21 nm s^{-1}, ArpC5A 22 nm s^{-1}). Those results were not a bias of the experimental spatial and temporal resolutions. Indeed, F-actin movements in small spine precursors, dendritic filopodia, were polarized rearward and faster than in spines (Fig 1C and D; actin 34 nm s^{-1}). In addition, CD treatment, which stops membrane protrusions in spines (Fischer *et al*, 1998; Dunaevsky *et al*, 1999), decreased the velocity of F-actin movements to the level measured in fixed cells (Fig 1C and D; actin 14 nm s^{-1}). Altogether, those results suggest that in spines, the slow and none polarized motions of branched F-actin networks may not be primarily driven by F-actin growth against protrusion tips.

Spine motility is supported by finger-like protrusions

There is an inverse relationship between the rate of F-actin flow and membrane protrusion (Giannone *et al*, 2004). Thus, the slow rate of F-actin and Arp2/3 complex movement implies that F-actin elongation will lead to efficient pushing forces triggering membrane protrusions and spine motility (Fischer *et al*, 1998; Dunaevsky *et al*, 1999; Lendvai *et al*, 2000; Berning *et al*, 2012). To determine the shape of membrane protrusions in spines, we acquired single-molecule-based super-resolution intensity images in live neurons using PALM (Betzig *et al*, 2006; Shroff *et al*, 2008). We used stronger laser illumination and fast acquisition frequency (100 Hz)

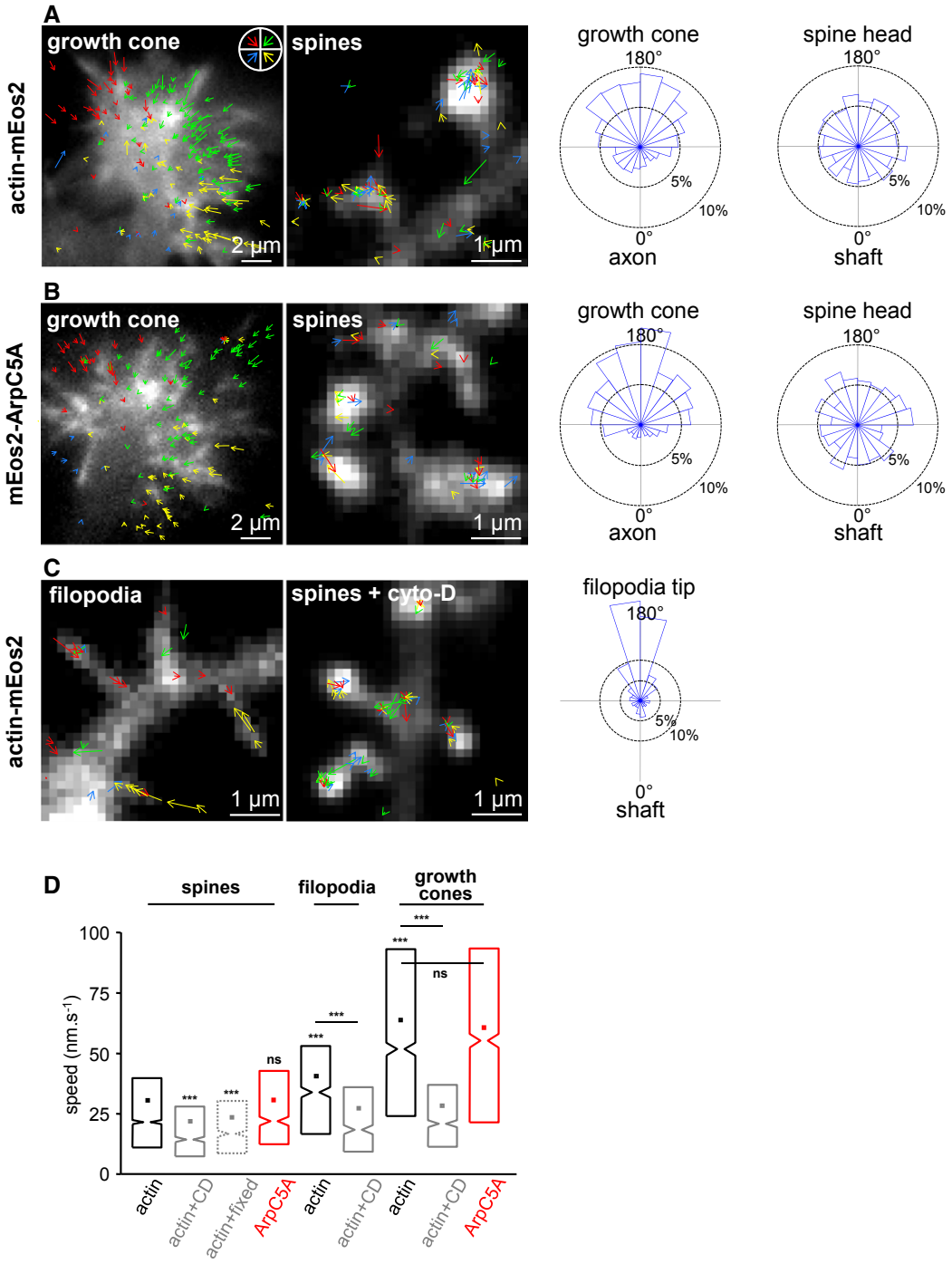

Figure 1. Arp2/3 complex and F-actin movements are not polarized in spines.

A Left panels: actin-mEOS2 trajectories acquired using low-frequency (2 Hz) sptPALM sequence in a growth cone (3–4 DIV) (left) and in spines (17–21 DIV) (right). Trajectories are represented by arrowheads starting at the beginning and finishing at the end of tracks. Arrowheads are color-coded to show their directions and superimposed on actin-mEOS2 low-resolution fluorescent image (gray scale). Scale bars, 2 µm (left), 1 µm (right). Right panels: polar histograms of the angular distribution of trajectories in growth cones (left) and dendritic spines (right).

B Same as (A) for mEOS2-ArpC5A.

C Left panels: same as (A) for actin-mEOS2 in dendritic filopodia (9–11 DIV) (left) and in spines (17–21 DIV) treated with CD (right). Scale bars, 1 µm. Right panel: polar histogram of the angular distribution of trajectories in dendritic filopodia.

D Box plots displaying the median (notch) and mean (square) ± percentile (25–75%) of speed distributions. All results for each condition correspond to pooled data from several independent experiments. Spines: actin (19 cells/2,665 trajectories), actin + CD (7/841), actin fixed (5/699), ArpC5A (4/665); filopodia: actin (7/730), actin + CD (6/512); growth cone: actin (11/1,699), actin + CD (4/780), ArpC5A (16/1,565). Where indicated, statistical significance was obtained using two-tailed, non-parametric Mann–Whitney rank sum test. The different conditions were compared with the spine actin condition. Otherwise, a black line indicates which conditions were compared. The resulting *P*-values are indicated as follows: ns, $P > 0.05$; ***$P < 0.001$.

to increase the rate of mEOS2 photobleaching and the frequency of localization. This protocol allowed localizing most mEOS2 molecules more rapidly (~80 s). Fast-moving mEOS2 outlined the spine shape, while confined and immobile mEOS2 accumulated in sub-spine domains (Fig 2). We used cytosolic mEOS2 as a volume reporter and actin-mEOS2 to localize the entire F-actin network (Fig 2A and Supplementary Fig S1A). Strikingly, ~70% of spines (141/203) that appeared globular or cup shaped when imaged at low resolution are in fact more complex structures composed of several finger-like extensions when imaged using super-resolution.

To determine whether those membrane extensions corresponded to protrusions powered by F-actin polymerization, we imaged F-actin elongators. VASP and FMNL2 elongate F-actin barbed ends and localize at the tips of plasma membrane protrusions including lamellipodia and filopodia (Rottner *et al*, 1999; Bear *et al*, 2002; Breitsprecher *et al*, 2011; Block *et al*, 2012). VASP is located in spines and regulates spine morphology and enlargement (Ackermann & Matus, 2003; Lin *et al*, 2010), and FMNL2 is strongly expressed in neurons (Gardberg *et al*, 2010). Live super-resolution intensity images showed that mEOS2-VASP and FMNL2-mEOS2 accumulated at the tips of the finger-like extensions in spines (Fig 2B and C). Time-lapse recordings demonstrated that those extensions corresponded to protrusions, lost after CD treatment, and moving forward with velocities close to the ones measured for lamellipodia and filopodia (~60 nm s^{-1}; 22 protrusions) (Svitkina *et al*, 2003; Giannone *et al*, 2004) (Supplementary Fig S2). We used direct stochastic optical reconstruction microscopy (dSTORM) (Van de Linde *et al*, 2011) and demonstrated that endogenous VASP and FMNL2 were also enriched at the tips of finger-like protrusions in spines (Supplementary Fig S1B and C). Thus, spine motility is supported by multiple finger-like protrusions driven by the polarized elongation of F-actin barbed ends.

F-actin elongators delocalize outwards from the PSD while nucleation factors localize at the PSD

To examine the distribution of F-actin elongators relative to the PSD, we performed sequential dual-color super-resolution microscopy using PALM for mEOS2-VASP and dSTORM for endogenous PSD-95 (Fig 3A). We quantified the scattering of PSD-95 within spines by measuring the distances of each detection from the centroid of all detections (see Materials and Methods). PSD-95 detections displayed low scattering within the spines (185 nm) and were mainly grouped into a single domain (long/short axis, 269/114 nm; see Materials and Methods) (Fig 3D and E). Consistent with live experiments, mEOS2-VASP invariably formed nano-domains (111/66 nm) at the tip of the finger-like protrusions (Fig 3A and D). Distances of mEOS2-VASP detections from the centroid of PSD-95 showed that VASP was mainly localized away from the PSD-95 domain (383 nm; Fig 3E). Thus, VASP-mediated elongation of F-actin barbed ends is frequently directed outwards from the PSD.

Working hypotheses on F-actin dynamics in spines were built in analogy with the lamellipodium (Hotulainen & Hoogenraad, 2010). In this structure, the WAVE complex that activates Arp2/3-mediated nucleation is localized, like VASP and FMNL2, at the tip of membrane protrusions (Miki *et al*, 2000; Innocenti *et al*, 2004; Steffen *et al*, 2004). The same organization in dendritic spines would imply that the WAVE complex is also localized at the tip of membrane protrusions. The WAVE complex is stable and composed of five proteins: WAVE, Abi, Nap, Brick and Sra (Gautreau *et al*, 2004; Lebensohn & Kirschner, 2009). WAVE and Abi1 are located in spines (Proepper *et al*, 2007; Soderling *et al*, 2007), consistent with the involvement of the WAVE complex in shaping dendritic spine morphology, synaptic plasticity and behavior (Soderling *et al*, 2003, 2007; Kim *et al*, 2006). We used mEOS2-Abi1 to determine the sub-spine localization of the WAVE complex. Surprisingly, dual-color PALM/dSTORM experiments demonstrated that mEOS2-Abi1 detections formed a domain having the same size (248/112 nm) and overlapping with the PSD-95 domain (Fig 3B, D and E). Likewise, live super-resolution intensity images showed that mEOS2-Abi1 was not localized at protruding tips, but clustered into a single domain (Supplementary Fig S3A and D). Since Abi1 could also be part of other protein complexes (Proepper *et al*, 2007), we performed experiments using Nap1, another subunit of the WAVE complex, to further support the nanoscale organization of the WAVE complex. Live super-resolution intensity images and dual-color PALM/dSTORM experiments demonstrated that mEOS2-Nap1, like mEOS2-Abi1, was not localized at protruding tips, but also clustered into a single central domain having the same size and overlapping with PSD-95 (Fig 3D and E, Supplementary Figs S3 and S5). Endogenous WAVE proteins, imaged using dSTORM, also displayed clusterization within the spine (Supplementary Fig S4A).

IRSp53, which binds and regulates the WAVE complex, also localizes at the tip of lamellipodia and filopodia (Miki *et al*, 2000; Nakagawa *et al*, 2003; Suetsugu *et al*, 2006). This membrane and F-actin binding protein encompasses an I-BAR domain binding to outwardly curved membrane protrusions (Scita *et al*, 2008). IRSp53 is concentrated in spines and regulates spine morphology (Bockmann *et al*, 2002; Choi *et al*, 2005). Live super-resolution intensity images and dual-color PALM/dSTORM experiments demonstrated that mEOS2-IRSp53 also formed a single domain co-localizing with PSD-95 (Supplementary Fig S6). These results suggest that a membrane domain apposed to the PSD is targeted by IRSp53 and the WAVE complex and is involved in the initiation of branched F-actin networks.

In lamellipodia, the Arp2/3 complex is incorporated in F-actin networks at the tip of membrane protrusions and flows inward from the tip (Iwasa & Mullins, 2007; Lai *et al*, 2008). The co-localization of PSD-95, the WAVE complex and IRSp53 at the center of the spine, together with the slow and unpolarized motions of branched F-actin networks (Fig 1), suggested that Arp2/3 nucleation is not occurring at protrusion tips in spines. Indeed, experiments performed with mEOS2-ArpC5A showed that Arp2/3 is forming multiple nano-domains (97/63 nm) partially over-lapping with PSD-95 (Fig 3C–E, Supplementary Figs S3 and S4). Altogether, our data support a model where branched F-actin networks are nucleated at or close to the PSD, providing barbed ends that are then elongated outwards from the PSD. This segregation clearly differs from the lamellipodium, where branched actin network nucleation and elongation both occur at the protrusion tip.

Cytosolic, freely diffusing Arp2/3 complexes become immobilized in F-actin networks within spines

The nucleation of F-actin branches requires the coordination in space and time of different signals involving the Arp2/3 complex,

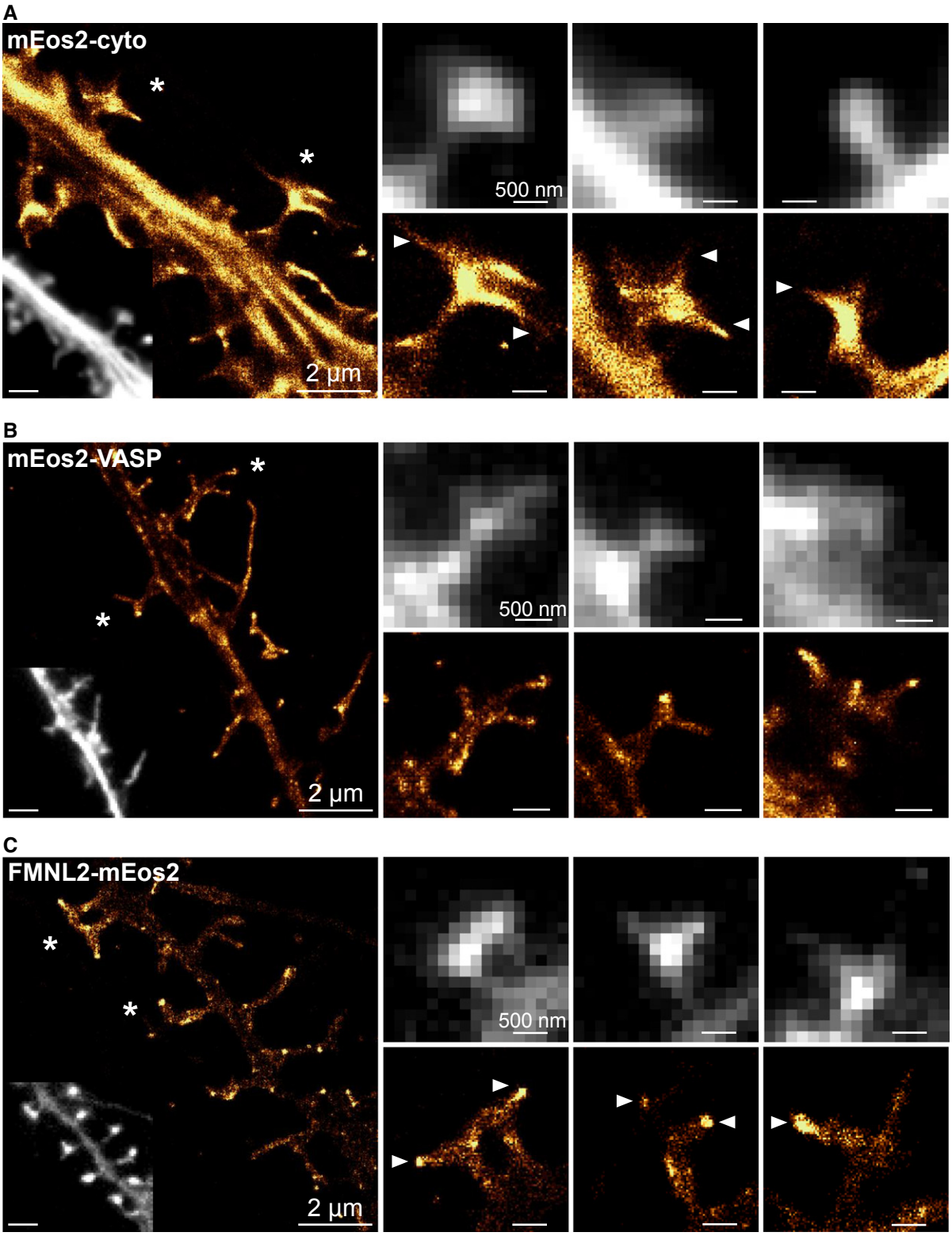

Figure 2. F-actin elongators localize at the tips of finger-like protrusions in spines.

A Super-resolution intensity image of cytosolic mEOS2 in a live neuron (17–21 DIV) obtained from a sptPALM sequence at high frequency (100 Hz) (inset: fluorescence image of mEOS2-cyto). Scale bars, 2 µm. Spines highlighted with a star (left) are shown on the right together with a spine belonging to another neuron. Scale bars, 500 nm. Arrowheads indicate examples of finger-like protrusions.

B Same as (A) for mEOS2-VASP. Arrowheads indicate VASP accumulations at protrusion tips.

C Same as (A) for FMNL2-mEOS2. Arrowheads indicate FMNL2 accumulations at protrusion tips.

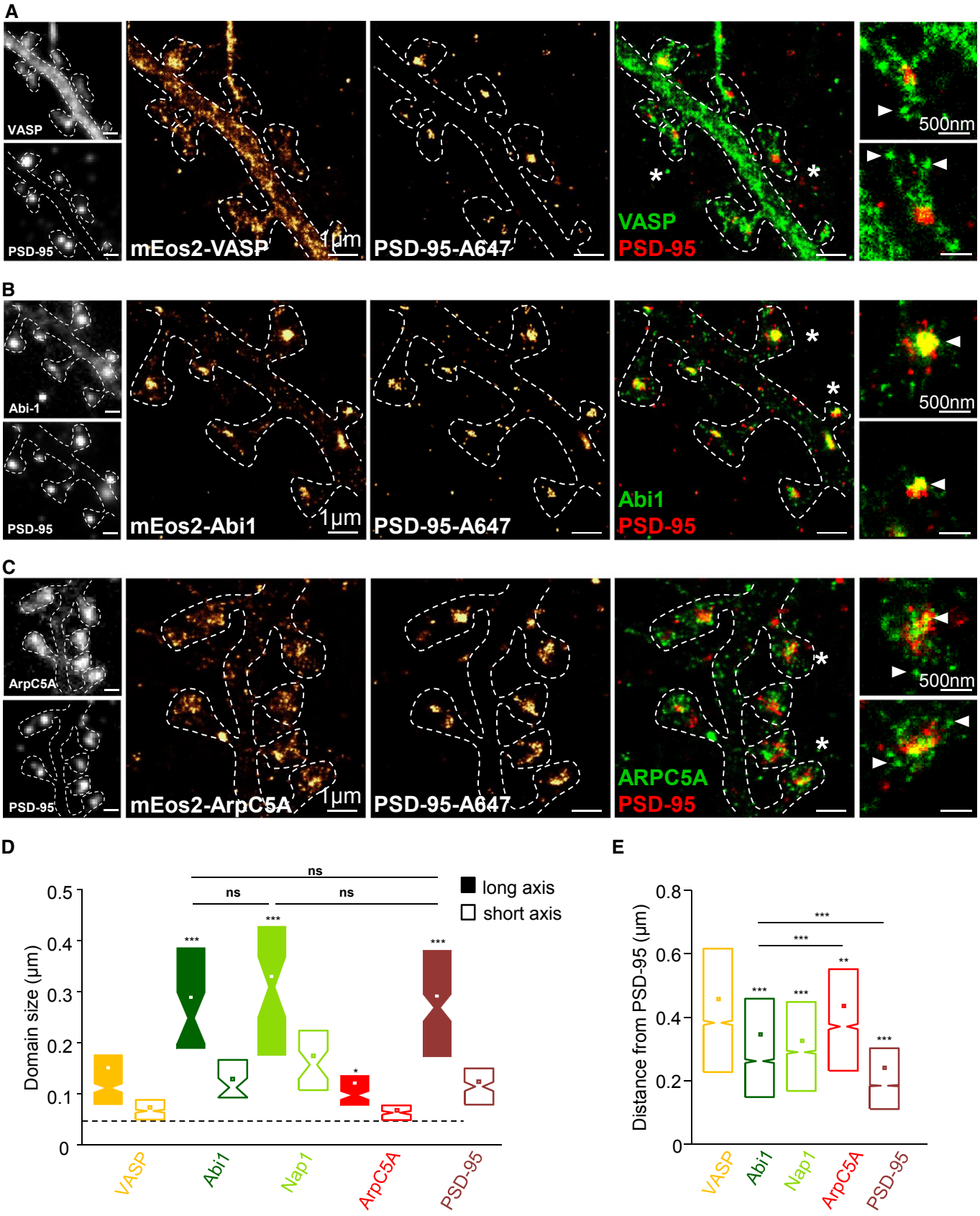

Figure 3.

the WAVE complex, IRSp53, acidic phospholipids (PIP3) and prenylated, GTP-bound Rac (Miki *et al*, 2000; Lebensohn & Kirschner, 2009; Chen *et al*, 2010). While super-resolution imaging allowed us to reveal the nanoscale organization of actin regulators, studying fast molecular dynamics is required to understand their coordination within spines. To determine the sequence of molecular events leading to Arp2/3 activation, we performed high-frequency sptPALM acquisition (20 Hz) to characterize the diffusive properties of actin regulators (Rossier *et al*, 2012). We reconstructed and analyzed thousands of trajectories of mEOS2-fused proteins in dendritic spines and shafts (Fig 4). For trajectories lasting more than 650 ms (> 13 points), we computed the mean-squared displacement (MSD), which describes the diffusion properties of a molecule. We sorted trajectories according to their diffusion modes (immobile, confined, free-diffusive; Fig 4B and H) and extracted the diffusion coefficients (D) (Fig 4G and I, Supplementary Table S1, see Materials and Methods) (Rossier *et al*, 2012). Within the spatial resolution of our experiments (~55 nm), all molecules with a D inferior to 0.004 $\mu m^2\ s^{-1}$ are classified as immobile.

The distribution of D showed that mEOS2-ArpC5A molecules were mainly immobile in spines (Fig 4G and H, 57 ± 3%), the remaining ones displaying either free-diffusion (Fig 4H and I, 19 ± 1%; $D_{diff} = 0.056\ \mu m^2\ s^{-1}$) or confined diffusion (Fig 4H, 24 ± 2%; $D_{conf} = 0.027\ \mu m^2\ s^{-1}$, Supplementary Table S1). The distribution of D for actin-mEOS2 was similar to that of Arp2/3 complex (Fig 4C, D and G), displaying a large fraction of immobilization in spines (56 ± 2%) (Fig 4H). These immobilization events correspond to fluorescent signals acquired using low-frequency acquisition (2 Hz) (Fig 1) and to nano-domains of Arp2/3 located on and around the PSD (Fig 3). Disruption of F-actin using Latrunculin A (LatA) induced loss of actin-GFP and GFP-ArpC5A accumulation in spines without disassembly of Homer1C-DsRed, used as a PSD reporter (Supplementary Fig S7A and B). LatA treatment induced a redistribution of D toward faster diffusions and lowered the fractions of immobilization for Arp2/3 complex and actin (Fig 4G-I and Supplementary Fig S8). Diffusion properties in LatA conditions tended toward values measured for cytosolic mEOS2 (Fig 4E–I and Supplementary Table S1), but did not reach the fast free-diffusion and low fraction of immobilization measured for mEOS2 anchored to the inner leaflet of the plasma membrane (mEOS2-CAAX; Fig 5E–I and Supplementary Table S1). Thus, in spines, Arp2/3 complexes are mainly incorporated into the F-actin network or freely diffusing in the cytosol as a dynamic pool readily available for new nucleation events. Our data show that Arp2/3 reaches the WAVE complex directly from the cytosol and not from the membrane as suggested for the lamellipodium of *Xenopus* XTC cells (Millius *et al*, 2012).

Abi1, Nap1 and IRSp53 are associated with confined components of the PSD

Association of the WAVE complex and IRSp53 with the plasma membrane coincides with Arp2/3 complex activation (Miki *et al*, 2000; Scita *et al*, 2008; Padrick & Rosen, 2010). To study the diffusion properties of WAVE complex subunits in spines, we performed sptPALM experiments using mEOS2-Abi1 and mEOS2-Nap1 (Fig 5A and B; Supplementary Fig S5C and D; Supplementary Table S1). Distributions of D were shifted toward faster diffusion compared to F-actin and Arp2/3 (Fig 5G; Supplementary Fig S5E; Supplementary Table S1). Both in shafts and in spines, the fractions of immobilized mEOS2-Abi1 and mEOS2-Nap1 were lower, and the fractions of confined and free-diffusion were larger (Fig 5H; Supplementary Fig S5F; Supplementary Table S1). In contrast to Arp2/3, which displayed transient immobilizations continually relocating in the spine, many confined and immobile mEOS2-Abi1 trajectories were detected in the same area (Fig 5B, Supplementary Fig S9A and B). Thus, those results suggest that the WAVE complex is retained in a confinement zone forming a long-lasting domain overlapping with the PSD.

In spines, IRSp53 displayed almost the same dynamics and subspine localization than WAVE complex subunits. Many confined trajectories formed a long-lasting domain of IRSp53 co-localizing with the PSD (Supplementary Figs S6 and S9C). In addition, mEOS2-IRSp53 displayed diffusion properties similar to mEOS2-Abi1 and mEOS2-Nap1 (Fig 5G–I, Supplementary Fig S5E–G), indicating that IRSp53 is confined in the same membrane domain. LatA treatment did not induce loss of Abi1 or IRSp53 accumulation in spines, which remained associated with the PSD (Supplementary Fig S7C and D), demonstrating that their recruitment in spines is not mediated by interactions with F-actin networks.

Figure 3. Actin nucleation and elongation factors are segregated within spines.

A Dual-color super-resolution images using sequential PALM and dSTORM of, respectively, mEOS2-VASP (left) and endogenous PSD-95 labeled with Alexa647 (PSD-95-A647; middle) in a fixed neuron. Merge (right). Scale bars, 1 μm. Left insets: fluorescence image of mEOS2-VASP (upper panel) and PSD-95-A647 (lower panel). Right insets: merge PALM/dSTORM of the spines highlighted by stars in the merged image. Scale bars (insets), 500 nm. Arrowheads indicate VASP accumulations at protrusion tips. Dotted lines were manually added to distinguish spine outlines and shafts.

B Same as (A) for dual-color mEOS2-Abi1 and PSD-95-A647. Arrowheads indicate Abi1 domain.

C Same as (A) for dual-color mEOS2-ArpC5A and PSD-95-A647. Arrowheads indicate examples of Arp2/3 nano-domains.

D Box plots displaying the median (notch) and mean (square) ± percentile (25–75%) of domain size for mEOS2-VASP (yellow, 5 cells, 53 spines, 402 domains), mEOS2-Abi1 (dark green, 4 cells, 36 spines, 39 domains), mEOS2-Nap1 (green, 4 cells, 46 spines, 46 domains), mEOS2-ArpC5A (red, 3 cells, 25 spines, 156 domains) and PSD-95-A647 (dark red, 16 cells, 145 spines, 157 domains). Long axis (solid box), short axis (open box). The dotted line corresponds to the size of isolated mEOS2 measured using Gaussian fitting (see Materials and Methods). Where indicated, statistical significance was obtained using non-parametric, two-tailed Mann–Whitney rank sum test; the different conditions were compared with the long axis of VASP condition. Otherwise, a black line indicates which conditions were compared. The resulting *P*-values are indicated as follows: ns, $P > 0.05$; *$P < 0.05$; ***$P < 0.001$.

E Box plots displaying the median and mean of distance distribution from the PSD-95 centroid for mEOS2-VASP (yellow, 5 cells, 42 spines, 7,653 detections), mEOS2-Abi1 (dark green, 4 cells, 44 spines, 6,749 detections), mEOS2-Nap1 (green, 4 cells, 61 spines, 7,377 detections), mEOS2-ArpC5A (red, 3 cells, 25 spines, 3,922 detections) and PSD-95-A647 (dark red, 16 cells, 162 spines, 20,249 detections). Where indicated, statistical significance was obtained using non-parametric, two-tailed Mann–Whitney rank sum test; the different conditions were compared with the VASP condition. Otherwise, black lines indicate which conditions were compared. The resulting *P*-values are indicated as follows: **$P < 0.01$; ***$P < 0.001$.

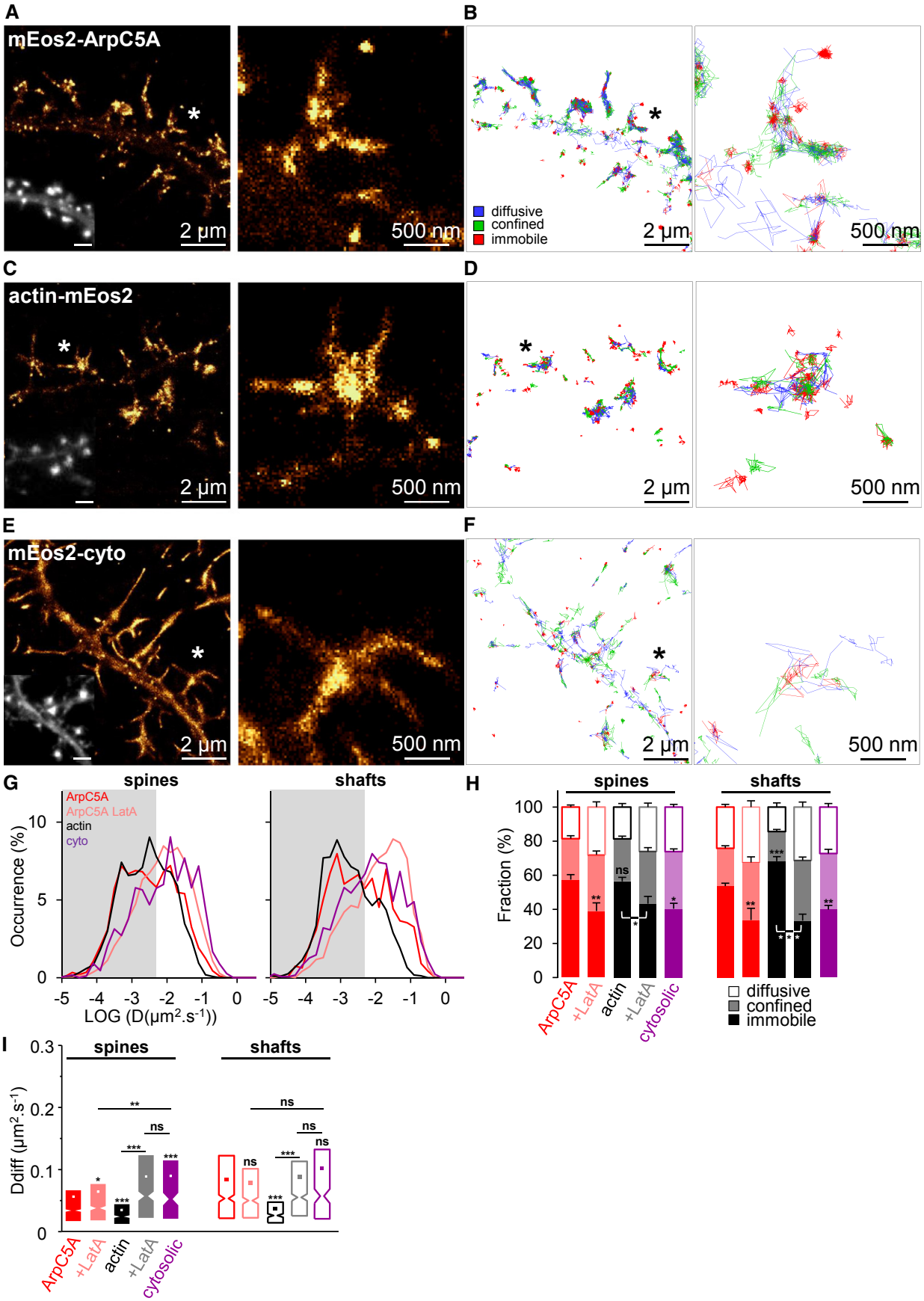

Figure 4.

Figure 4. Arp2/3 complex diffuses in the cytosol and becomes immobilized in F-actin networks.

A Super-resolution intensity image of mEOS2-ArpC5A in a neuron obtained from a sptPALM sequence (20 Hz, duration: 600 s; inset: fluorescence image of mEOS2-ArpC5A). Scale bars, 2 μm. Spine highlighted with a star (left) is shown on the right. Scale bar, 500 nm.

B Corresponding trajectories are color-coded to show their diffusion modes: diffusive (blue), confined (green) and immobile (red). Scale bars, 2 μm. Spine highlighted with a star (left) is shown on the right. Scale bar, 500 nm.

C, D Same as (A) and (B) for actin-mEOS2.

E, F Same as (A) and (B) for mEOS2-Cyto.

G Distribution of LOG(D) for mEOS2-ArpC5A (red), mEOS2-ArpC5A + LatA (pink), actin-mEOS2 (black) and mEOS2-cyto (purple) in spines (left) and shafts (right; mean for cells). The gray areas including D values inferior to 0.004 $\mu m^2 s^{-1}$ correspond to immobile trajectories.

H, I Fraction of diffusive, confined and immobile populations in spines (left) and shafts (right), mean ± SEM for cells (H). Diffusion coefficients (D) for free-diffusive trajectories in spines (left) and shafts (right) were represented by box plots (I) displaying the median (notch) and mean (square) ± percentile (25–75%). All results for each condition correspond to pooled data from several independent experiments (cells/trajectories): ArpC5A (11/11,097), ArpC5A + LatA (6/4,464), actin (4/6,113), actin + LatA (4/3,807) and cytosolic (3/1,700). Where indicated, statistical significance was obtained using two-tailed unpaired *t*-test for fractions of immobilization (H) or non-parametric, two-tailed Mann–Whitney rank sum test for diffusion coefficient (I). For spines and shafts, the different conditions were compared with the respective ArpC5A condition. Otherwise, a black line indicates which conditions were compared. The resulting *P*-values are indicated as follows: ns, $P > 0.05$; *$P < 0.05$; **$P < 0.01$; ***$P < 0.001$.

PSD-95 recruitment and nanoscale organization at the PSD also requires its association with the membrane through palmitoylation (Craven *et al*, 1999; Sturgill *et al*, 2009; Fukata *et al*, 2013; Zhang *et al*, 2014). The diffusive properties of mEOS2-PSD-95 in spines were similar to Abi1, Nap1 and IRSp53 (Fig 5C, D, G–I), being also dominated by a long-lasting domain of confined and immobile trajectories (Supplementary Fig S9D), suggesting that those proteins are sequestered in the same membrane domain. Glutamate AMPA receptors (GluA) are recruited to the PSD by a diffusion/immobilization mechanisms (Bats *et al*, 2007). However, in contrast to Abi1, Nap1, IRSp53 and PSD-95, GluA receptors form long-lasting nanodomains composed of only immobilized receptors partially overlapping with PSD-95 (Nair *et al*, 2013). Thus, the membrane apposed to the PSD, like the lamellipodium tip, could be a domain where IRSp53 and the WAVE complex are confined, regulating or mediating Arp2/3 activation.

Rac1 reaches the PSD by membrane free-diffusion

In agreement with the involvement of Arp2/3 in determining the shape of dendritic spines, gain and loss of the Rac1 GTPase activity induce, respectively, spine growth and shrinkage and are also correlated with enhanced and decreased motility (Tashiro & Yuste, 2004). Rac1 is targeted to the plasma membrane where it activates the WAVE complex and consequently Arp2/3-dependent nucleation (Lebensohn & Kirschner, 2009; Chen *et al*, 2010). Accordingly, the diffusive properties of mEOS2-Rac1 in spines and shafts were almost identical to mEOS2-CAAX (Fig 6A, B, G–I and Supplementary Table S1), showing that Rac1 was freely diffusing at the membrane. The higher fraction of free-diffusion and faster free-diffusion of mEOS2-Rac1 in spines compared to WAVE complex subunits and IRSp53 is surprising given their direct interactions (Suetsugu *et al*, 2006). Those results suggested either that Rac1 binding to the WAVE complex is faster than our acquisition frequency or that such events are infrequent. To increase Rac1 activation, we used a constitutively active mutant, mEOS2-Rac1-Q61L, which is locked in the GTP-bound state. Strikingly, mEOS2-Rac1-Q61L was strongly immobilized both in spines and in shafts (Fig 6C and D). Distributions of D were shifted toward slower diffusion, fractions of immobilization were increased close to values measured for F-actin and Arp2/3 complex, and free-diffusions were drastically slowed down (Fig 6G–I). Thus, Rac1 activation is correlated with Rac1 membrane immobilization, only detectable in our experimental conditions when Rac1 is locked in its active state. A dominant-negative mutant, mEOS2-Rac1-T17N, exhibited the same diffusive properties as wild-type Rac1 (Fig 6E–I). Nevertheless, expression of mEOS2-Rac1-T17N induced the transformation of spines into filopodia-like structures (Fig 6E), indicating that even transient Rac1 immobilizations and activations are critical to maintain the globular spine shape. Thus, these results indicate that Rac1 reaches the membrane apposed to the PSD through membrane free-diffusion to transiently bind its targets such as the WAVE complex.

Dendritic spine enlargement is associated with delocalization of Abi1 from the PSD

Spine morphological remodeling is triggered by changes in F-actin polymerization (Okamoto *et al*, 2004) and may thus be associated with reorganization of F-actin regulators within spines (Park *et al*, 2012; Bosch *et al*, 2014). To test this hypothesis, we induced spine enlargement by enhancing Rac1 or Shank3 functions. We co-transfected constitutively active Rac1-Q61L with proteins fused to mEOS2, and performed sequential dual-color PALM/dSTORM experiments. Over-expression of cerulean-Rac1-Q61L induced profound morphological alterations of spines, being either transformed into large spines (Fig 7A) (Tashiro & Yuste, 2004) or merged into lamellipodia-like extensions (Supplementary Fig S10). Strikingly, mEOS2-Abi1 was still present in spines but delocalized from the PSD-95 (Fig 7A and C). In lamellipodia-like structures, mEOS2-Abi1 and mEOS2-VASP localized to the tip of membrane extensions, matching their organization in lamellipodia (Supplementary Fig S10). Shank3 is a PSD scaffold that directly interacts with a Rac1 activator and subunits of the Arp2/3 and WAVE complexes (Han *et al*, 2013). Its over-expression in neurons induces spine enlargement and enhanced F-actin content in spines (Sala *et al*, 2001; Durand *et al*, 2012; Han *et al*, 2013). We found that Shank3-GFP over-expression also triggered redistribution of mEOS2-Abi1 away from the PSD-95 (Fig 7B and C). Thus, our data suggest that in resting conditions, a critical upstream activator of Arp2/3, the WAVE complex, is sequestered close to the PSD preventing the formation of large protrusions (Fig 8). However, transient or long-lasting delocalization of the WAVE complex from the PSD could promote Arp2/3 activation and F-actin elongation throughout the spine, thereby triggering morphological remodeling.

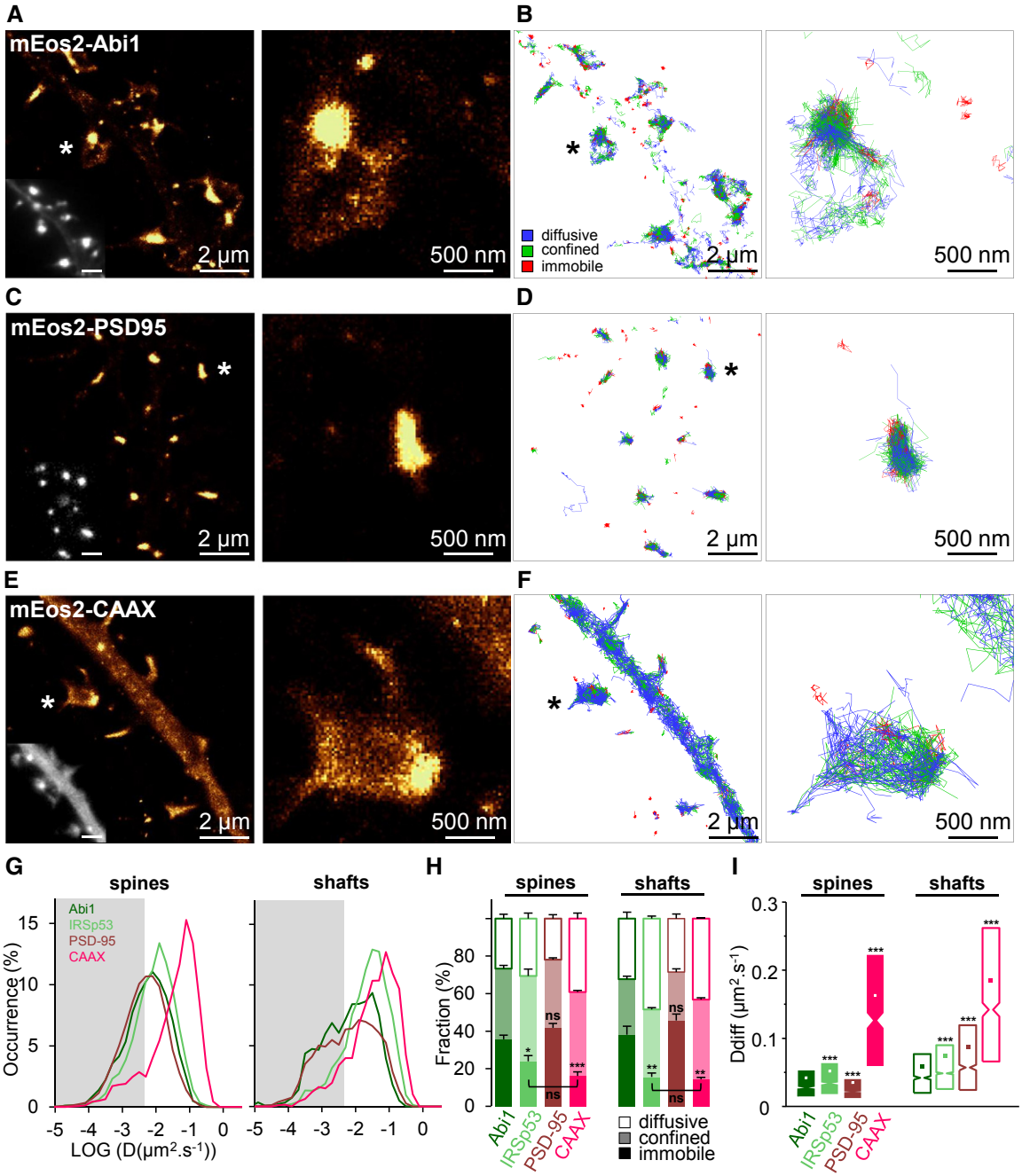

Figure 5. Abi1, IRSp53 and PSD-95 are confined at the PSD.

A Super-resolution intensity image of mEOS2-Abi1 in a neuron obtained from a sptPALM sequence (20 Hz, duration: 600 s; inset: fluorescence image of mEOS2-Abi1). Scale bars, 2 µm. Spine highlighted with a star (left) is shown on the right. Scale bar, 500 nm.

B Corresponding trajectories are color-coded to show their diffusion modes: diffusive (blue), confined (green) and immobile (red). Scale bars, 2 µm. Spine highlighted with a star (left) is shown on the right. Scale bar, 500 nm.

C, D Same as (A) and (B) for mEOS2-PSD95.

E, F Same as (A) and (B) for mEOS2-CAAX.

G Distribution of LOG(D) for mEOS2-Abi1 (dark green), mEOS2-IRSp53 (light green), mEOS2-PSD95 (dark red) and mEOS2-CAAX (magenta) in spines (left) and shafts (right), mean for cells. The gray areas including D values inferior to 0.004 $\mu m^2\ s^{-1}$ correspond to immobile trajectories.

H, I Fraction of diffusive, confined and immobile populations in spines (left) and shafts (right), mean ± SEM for cells (H). Diffusion coefficients (D) for free-diffusive trajectories in spines (left) and shafts (right) were represented by box plots (I) displaying the median (notch) and mean (square) ± percentile (25–75%). All results for each condition correspond to pooled data from several independent experiments (cells/trajectories): Abi1 (7/11,885), IRSp53 (5/17,974), PSD-95 (8/33,963) and CAAX (3/3,549). Where indicated, statistical significance was obtained using two-tailed unpaired *t*-test for fractions of immobilization (H) or non-parametric, two-tailed Mann–Whitney rank sum test for diffusion coefficient (I). For spines and shafts, the different conditions were compared with the respective Abi1 condition. Otherwise, a black line indicates which conditions were compared. The resulting *P*-values are indicated as follows: ns, $P > 0.05$; *$P < 0.05$; **$P < 0.01$; ***$P < 0.001$.

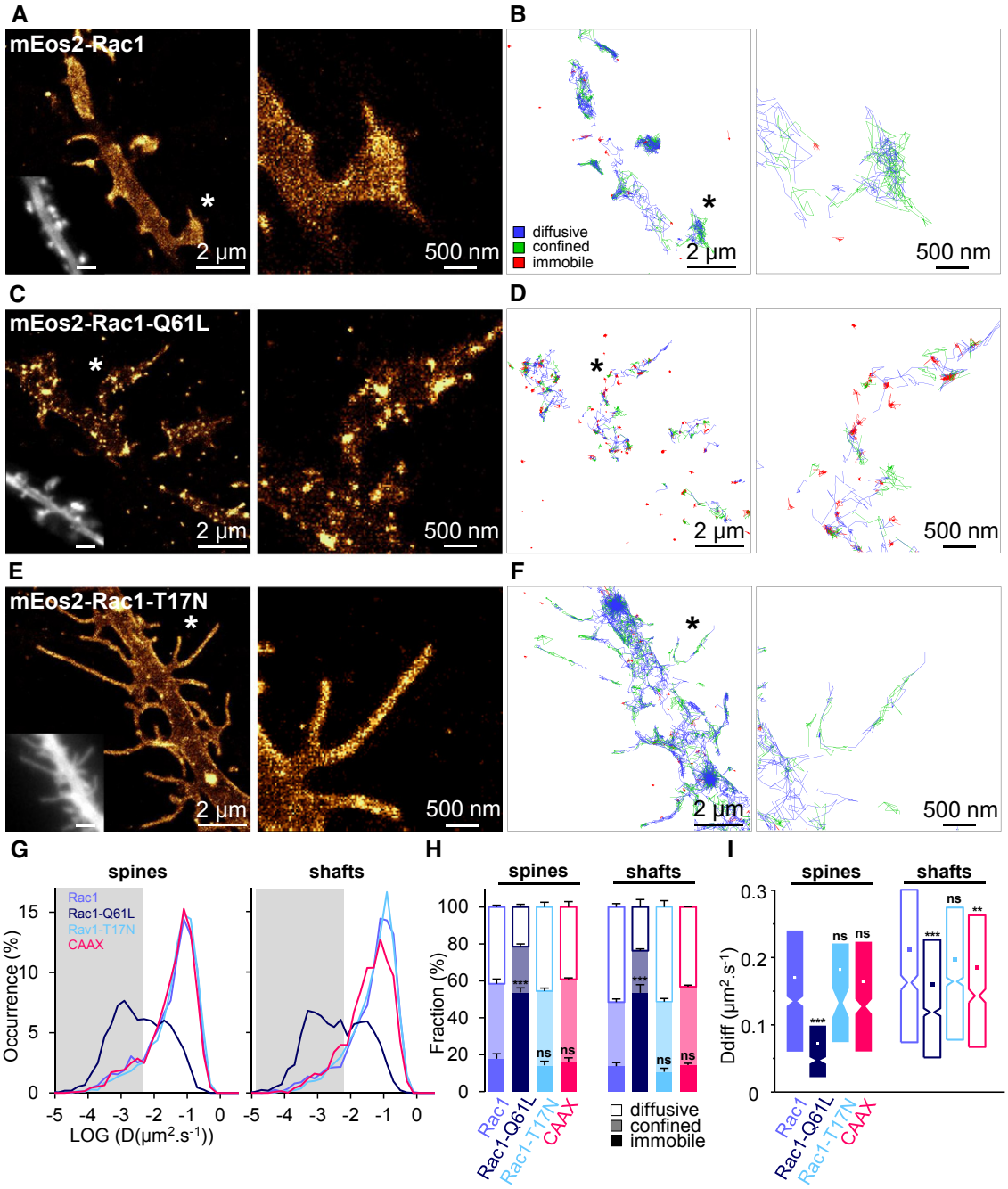

Figure 6. Rac1 activation is correlated with its membrane immobilization.

A Super-resolution intensity image of mEOS2-Rac1 in a neuron obtained from a sptPALM sequence (20 Hz, duration: 600 s; inset: fluorescence image of mEOS2-Rac1). Scale bars, 2 µm. Spine highlighted with a star (left) is shown on the right. Scale bar, 500 nm.

B Corresponding trajectories are color-coded to show their diffusion modes: diffusive (blue), confined (green) and immobile (red). Scale bars, 2 µm. Spine highlighted with a star (left) is shown on the right. Scale bars, 500 nm.

C, D Same as (A) and (B) for mEOS2-Rac1-Q61L.

E, F Same as (A) and (B) for mEOS2-Rac1-T17N.

G Distribution of LOG(D) for mEOS2-Rac1 (blue), mEOS2-Rac1-Q61L (dark blue), mEOS2-Rac1-T17N (light blue) and mEOS2-CAAX (magenta) in spines (left) and shafts (right), mean for cells. The gray areas including D values inferior to 0.004 $\mu m^2\ s^{-1}$ correspond to immobile trajectories.

H, I Fraction of diffusive, confined and immobile populations in spines (left) and shafts (right), mean ± SEM for cells (H). Diffusion coefficients (D) for free-diffusive trajectories in spines (left) and shafts (right) were represented by box plots (I) displaying the median (notch) and mean (square) ± percentile (25–75%). For comparison, the CAAX data from Fig 5G–I are shown again. All results for each condition correspond to pooled data from several independent experiments (cells/trajectories): Rac1 (4/5,896), Rac1-Q61L (5/5,514) and Rac1-T17N (6/8,759). Where indicated, statistical significance was obtained using two-tailed unpaired *t*-test for fractions of immobilization (H) or non-parametric, two-tailed Mann–Whitney rank sum test for diffusion coefficient (I). For spines and shafts, the different conditions were compared with the respective Rac1 condition. The resulting *P*-values are indicated as follows: ns, $P > 0.05$; $^{**}P < 0.01$; $^{***}P < 0.001$.

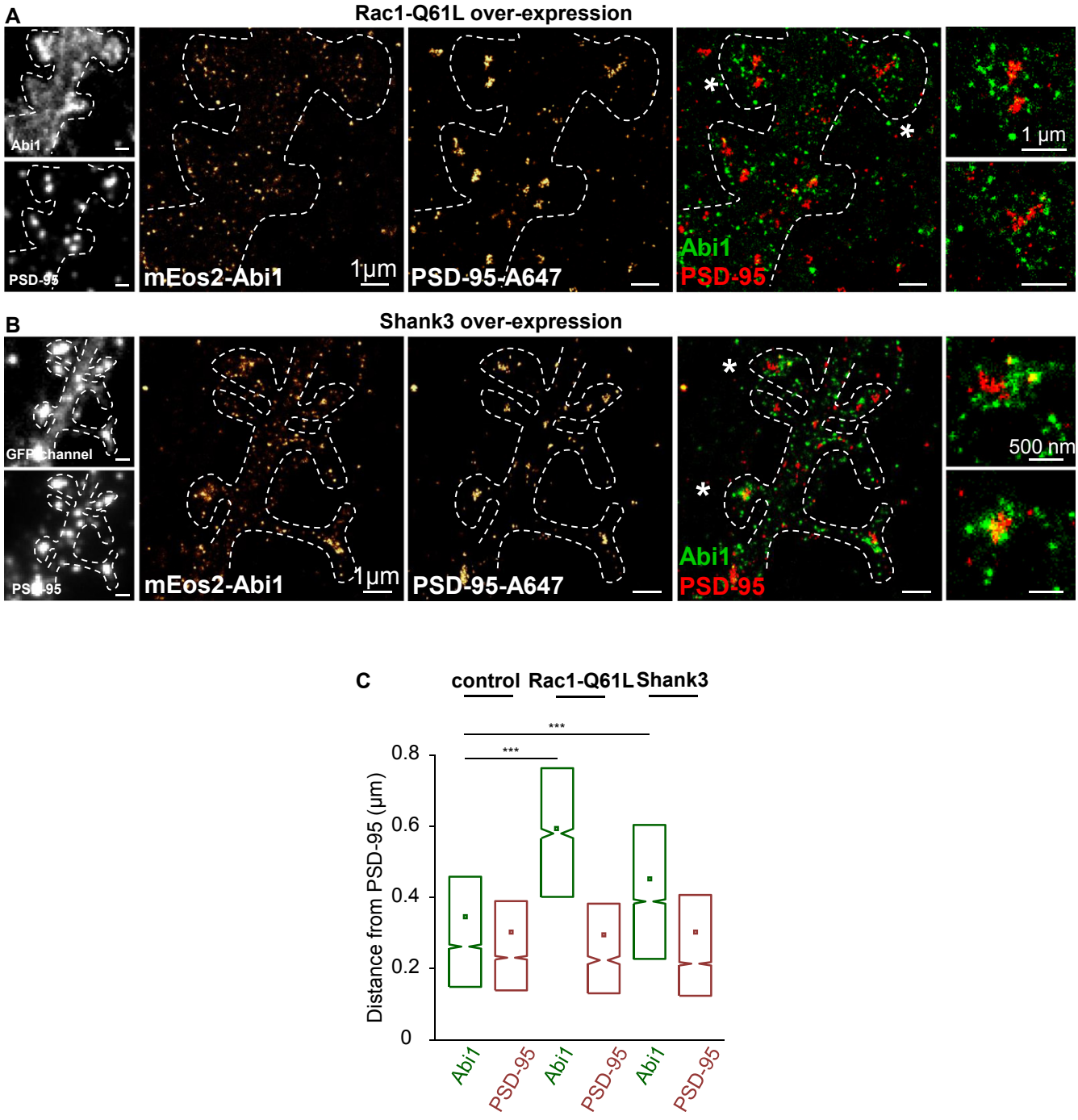

Figure 7. Rac1 enhanced activity and Shank3 over-expression delocalizes Abi1 from the PSD.

A Dual-color super-resolution images using sequential PALM and dSTORM of, respectively, mEOS2-Abi1 (left) and endogenous PSD-95 labeled with Alexa647 (middle) in a fixed neuron expressing cerulean-Rac1-Q61L. Merge (right). Scale bars, 1 µm. Left insets: fluorescence image of mEOS2-Abi1 (upper panel) and PSD-95-A647. Right insets: merge PALM/dSTORM of spines marked by stars in the merged image. Scale bars (insets), 1 µm. Dotted lines were manually added to distinguish spine outlines and shafts.

B Same as (A) for a neuron expressing Shank3-GFP. Merge (right). Scale bars, 1 µm. Left insets: fluorescence image of mEOS2-Abi1 and Shank3-GFP (upper panel) and PSD-95-A647 (lower panel). Right insets: merge PALM/dSTORM of spines marked by stars in the merged image. Scale bars (insets), 500 nm. Dotted lines were manually added to distinguish spine outlines and shafts.

C Box plots displaying the median and mean of distance distribution from the PSD-95 centroid for mEOS2-Abi1 and PSD95-A647 in control cells (4 cells, 44 spines, 6,749 detections for Abi1 and 6,183 detections for PSD95), in cells expressing cerulean-Rac1-Q61L (2 cells, 12 spines, 1,866 detections for Abi1 and 1,275 detections for PSD95) and in cells expressing Shank3-GFP (green, 6 cells, 62 spines, 9,101 detections for Abi1 and 9,469 detections for PSD95). For comparison, the mEOS2-Abi1 data from Fig 3E are shown again. Black lines indicate which conditions were compared; statistical significances were obtained using non-parametric, two-tailed Mann–Whitney rank sum test. The resulting *P*-values are indicated as follows: ***$P < 0.001$.

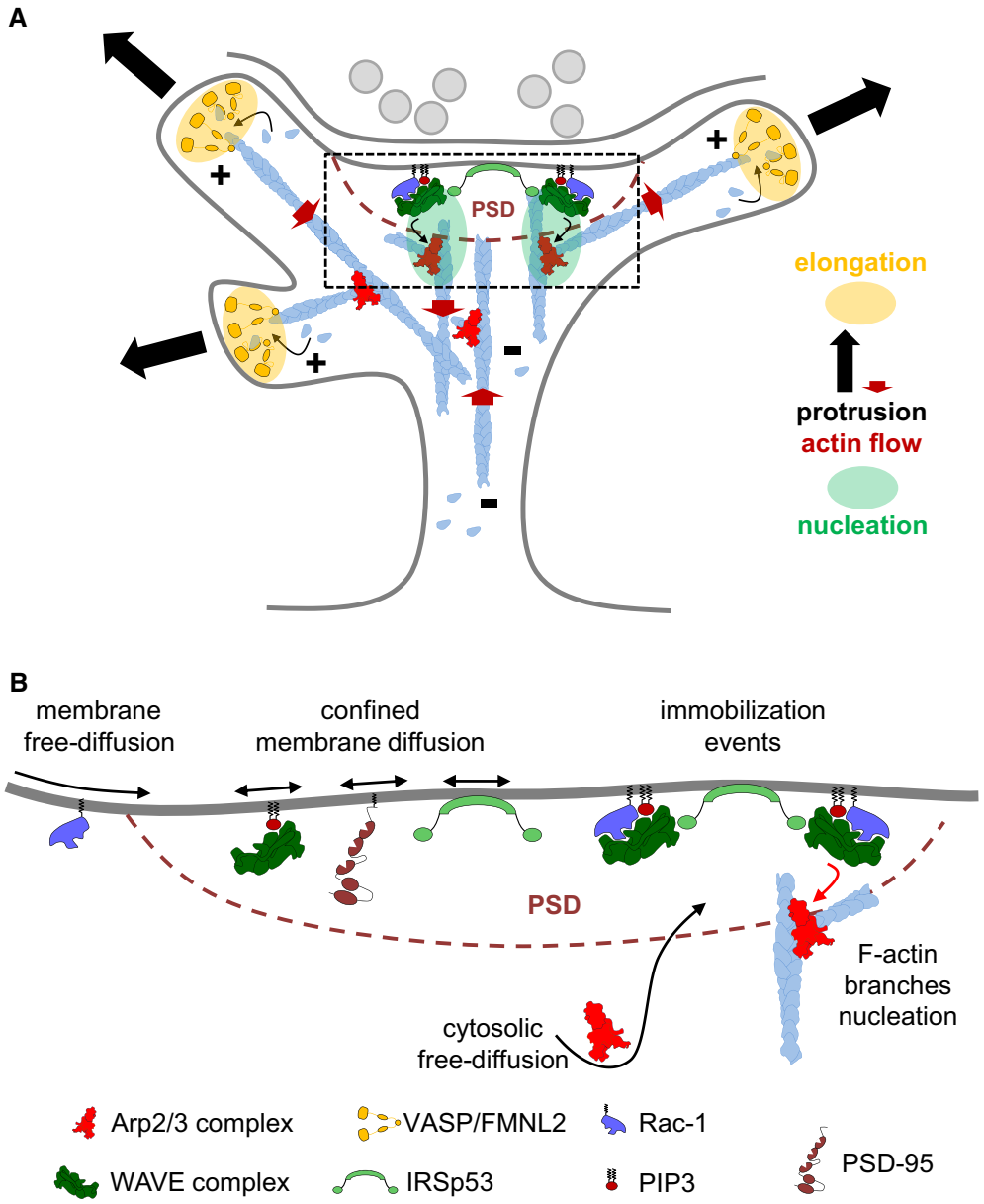

Figure 8. The dynamic nanoscale segregation of branched F-actin nucleation and elongation determines dendritic spine shape.
Schematic representation of the dynamic nanoscale organization of branched F-actin regulators in spines.

A Nucleation and elongation are not colocalized in dendritic spines. Nucleation of branched F-actin networks occurs close to the PSD, which is consistent with Arp2/3 complex immobilizations distributed around the PSD, and the co-localization of WAVE complex subunits and IRSp53 with PSD-95. However, growing F-actin barbed ends (+) are located at the tips of membrane protrusions, where elongation of F-actin is catalyzed by VASP and FMNL2. In this model, elongation from immobile Arp2/3 close to the PSD will not generate a concerted fast rearward flow of Arp2/3 complex and F-actin in spines.

B The PSD is the convergence zone where proteins triggering branched F-actin nucleation meet with the highest probability. The PSD is a persistent confinement zone for the WAVE complex and IRSp53. Rac1 GTPase reaches the PSD by membrane free-diffusion, its immobilization being correlated with its activation. Arp2/3 reaches the vicinity of the PSD by cytosolic free-diffusing where it becomes immobilized in F-actin networks.

Discussion

We present evidence to support a precise spatial segregation between regulators triggering nucleation and elongation of branched F-actin networks within dendritic spines. We also demonstrate that this nanoscale organization of F-actin regulators could be modulated in concert with changes in spine morphology. Our results identify the PSD as a critical organizing center of branched F-actin regulators in spines. Thus, the spatiotemporal control of interaction between PSD components and F-actin regulators might be at the basis of actin remodeling often associated with synaptic plasticity and abnormal spine morphologies in neurological disorders.

The architecture and polarity of F-actin networks in spines are still undefined. First, ensemble measurement using fluorescence

recovery after photobleaching or photoactivation showed that F-actin in spines is composed of dynamic and stable pools (Star *et al*, 2002; Honkura *et al*, 2008). Therefore, a unique polarity is probably unlikely. Second, electron microscopy (EM) micrographs, based on thin spine sectioning, gave an incomplete picture of F-actin networks. Those studies often focused on F-actin and actin binding proteins localized in the spine cytoplasm between the PSD and the shaft (Rácz *et al*, 2013). Within this region, early EM studies showed that F-actin barbed ends could contact the PSD, implying that pointed ends are directed toward the shaft (Fifkova & Delay, 1982). This orientation is consistent with F-actin movements directed from the PSD toward the shaft (Frost *et al*, 2010). However, EM micrographs also demonstrated the existence of thin protrusions emerging from the spine head named spinules (Spacek & Harris, 2004) that could correspond to F-actin membrane protrusions (Edwards, 1998; Fischer *et al*, 1998; Izeddin *et al*, 2011; Berning *et al*, 2012; Ueda & Hayashi, 2013). Our data reveal that finger-like protrusions responsible for spine motility are powered by the polarized elongation of F-actin barbed ends away from the PSD. Increased or decreased Rac1 activity induced the conversion of spines into non-motile or lamellipodia-like structures, respectively, supporting the hypothesis that spine protrusions are emerging from elongation of branched F-actin networks.

Nucleation and elongation of F-actin are co-localized at the lamellipodium tip, triggering an inward growth of branched F-actin networks. The location of the WAVE complex, IRSp53, VASP, FMNL2 and fast-growing F-actin barbed ends at protrusion tips supports that model (Lanier *et al*, 1999; Rottner *et al*, 1999; Nakagawa *et al*, 2003; Iwasa & Mullins, 2007; Lai *et al*, 2008; Block *et al*, 2012). Our results provide evidence that in spines, elongation and nucleation zones are not co-localized (Fig 8A). The tips of actin-driven membrane protrusions are enriched in VASP and FMNL2, indicating that they contain fast-growing F-actin barbed ends. However, the WAVE complex subunits Abi1 and Nap1 along with IRSp53 are retained close to the PSD. In addition, Arp2/3 complex immobilizations on F-actin networks are partially co-localizing with the PSD. Consistent with retention close to the PSD, Abi1, IRSp53 and Arp2/3 are directly and indirectly binding to PSD components, including CAMKII, Shank1, Shank3 and PSD-95 (Bockmann *et al*, 2002; Hering & Sheng, 2003; Choi *et al*, 2005; Proepper *et al*, 2007; Park *et al*, 2012; Han *et al*, 2013). Elongation from immobile Arp2/3 close to the PSD will not generate a concerted, fast rearward flow of Arp2/3 complex and F-actin, consistent with our results and previous studies on actin dynamics (Tatavarty *et al*, 2009, 2012). Nevertheless, this is not in disagreement with studies describing slow rearward movements of F-actin in spines (Honkura *et al*, 2008; Frost *et al*, 2010). Indeed, those backward movements might result either from F-actin severed from protrusions that could be recycled at the spine center to prime new nucleation events (Achard *et al*, 2010) or from protrusions ruffling back to the spine center (Berning *et al*, 2012). Consistent with the absence of a fast, concerted F-actin flow, a significant fraction of F-actin photoactivated at the spine apex remained at its initial position tens of seconds after photoactivation (Honkura *et al*, 2008), as opposed to similar experiments performed in the lamellipodium (Lai *et al*, 2008). This opposite organization compared to classical protrusive structures might rely on specific biophysical properties of the PSD. In contrast to nucleation zones moving with protrusion tips, the membrane juxtaposed to the PSD could represent a stationary nucleation zone, held in place by synaptic components such as scaffolding and adhesion proteins (Sheng & Hoogenraad, 2007). The demonstration of a direct interaction between the synaptic adhesion proteins Neuroligins and the WAVE complex reinforces our model (Chen *et al*, 2014). Furthermore, the densely packed PSD architecture (Sheng & Hoogenraad, 2007) could be a physical barrier forcing F-actin barbed ends to grow away. Consistent with this hypothesis, an *in vitro* reconstituted system demonstrated that F-actin branched networks could elongate with barbed ends growing away from a nucleating surface (Achard *et al*, 2010). Thus, we propose that in spines, branched F-actin networks are nucleated close to the PSD and elongate away from the PSD (Fig 8A).

Activation of the Arp2/3 complex is the final step of synchronized events occurring at the membrane and involving prenylated Rac-GTP, PIP3, the WAVE complex and IRSp53 (Miki *et al*, 2000; Lebensohn & Kirschner, 2009; Chen *et al*, 2010). Our study demonstrates that the zone of highest convergence between major effectors of Arp2/3 activation is the membrane juxtaposed to the PSD (Fig 8B). Several results suggest that IRSp53 and the WAVE complex are confined in the same membrane domain in spines. On the contrary to Arp2/3 that is immobilized in nano domains, IRSp53 and the WAVE complex subunits Abi1 and Nap1 are concentrated in a stable domain overlapping with PSD-95 and display a large fraction of confined diffusion. These diffusive properties are shared by PSD-95, which directly interacts with IRSp53 and also requires membrane targeting to fulfill its functions (Craven *et al*, 1999; Choi *et al*, 2005; Scita *et al*, 2008; Sturgill *et al*, 2009; Padrick & Rosen, 2010; Fukata *et al*, 2013; Zhang *et al*, 2014). Furthermore, Abi1 and IRSp53 are retained at the PSD after F-actin network disruption. Free-diffusion on the membrane was reported for WAVE2 and Arp2/3 in the lamellipodium of *Xenopus* XTC cells, which could increase the probability of their association (Millius *et al*, 2012). However, our results support the view that in neurons, Arp2/3 is reaching the PSD domain directly by free-diffusion from the cytosol. Since WAVE complex and IRSp53 oligomerization were proposed to increase Arp2/3-dependent nucleation (Padrick & Rosen, 2010), their concentration at the PSD could constitute a docking site for efficient Arp2/3 activation. Experiments using constitutively active Rac1-Q61L showed that Rac1 activation is correlated with its immobilization, in agreement with a recent study performed on adhesion sites of motile cells (Shibata *et al*, 2013). The large fraction of fast membrane free-diffusion for Rac1 wild-type compared to Abi1 and Nap1 suggests that Rac1 interacts only transiently with the WAVE complex, consistent with their low binding affinity (Chen *et al*, 2010; Koronakis *et al*, 2011). Therefore, Rac1 could diffuse in the membrane apposed to the PSD to transiently bind and activate stationary or confined WAVE complexes. Altogether, our results indicate that in spines, the PSD behaves as an organizing center of branched F-actin nucleation.

Changes in spine shape occur at different timescales, from the long-lasting morphologies acquired during developmental spine maturation (Govek *et al*, 2005; Charrier *et al*, 2012) to the acute remodeling that occur during synaptic plasticity (Matsuzaki *et al*, 2004). Importantly, abnormal spine maturation and morphologies are often associated with neurological disorders and genetic

deregulation of proteins impacting on the branched F-actin network. These include proteins signaling to the WAVE and Arp2/3 complexes, like Rac1 GAPs and GEFs, or proteins such as Shank3 and FMRP which directly interact with subunits of those complexes (Schenck *et al*, 2003; Govek *et al*, 2005; Penzes *et al*, 2011; Durand *et al*, 2012; Han *et al*, 2013; De Rubeis *et al*, 2013). Our results show that long-lasting enhancement of Rac1 or Shank3 functions, which trigger spine enlargement, is correlated with delocalization of the WAVE complex from the PSD. However, acute activation of F-actin regulatory proteins is also necessary to trigger and maintain spine enlargement during structural synaptic plasticity (Okamoto *et al*, 2009; Bosch *et al*, 2014). Rho GTPases including RhoA, Cdc42 and Rac1 are at the convergence of various signaling pathways triggered by CAMKII following enhanced synaptic activity (Murakoshi *et al*, 2011). Our results show that WAVE complex subunits and IRSp53, which operate in Rac1 signaling to Arp2/3, are sequestered close to the PSD where they are ideally located to be efficiently modulated by changes in synaptic activity. Accordingly, in resting conditions, CAMKII interacts with Abi1 resulting in a mutual inhibition. Active CAMKII phosphorylates and releases Abi1, which as part of the WAVE complex is then available to potentially activate Arp2/3 (Park *et al*, 2012). In addition, inactive CAMKII bundles and stabilizes F-actin, while its activation disrupts their association, allowing enhanced F-actin remodeling (Okamoto *et al*, 2007; Lin & Redmond, 2008). Importantly, increased recruitment and transient activation of cofilin occur in spines during the first phase of LTP, allowing a short time window for F-actin remodeling (Bosch *et al*, 2014). Thus, it is plausible that alteration of spine morphology could rely on the long-lasting or transient nanoscale relocalization of branched F-actin regulators, for example, the WAVE complex, leading to remodeling of the entire dendritic spine structure. Yet, the precise sequence of molecular events leading to reorganization of F-actin regulators within spines during synaptic plasticity or neurological disorders remains an open question. Nevertheless, our findings on the dynamic organization of branched F-actin regulators provide a framework to unravel the molecular mechanisms triggering remodeling of F-actin architecture during changes of spine morphology.

Materials and Methods

Cell culture

Preparation of cultured neurons was performed as previously described (Mondin *et al*, 2011). Dissociated hippocampal neurons from 18-day-old rat (Sprague Dawley) embryos were cultured on glass coverslips following the Banker protocol. The experimental ethical committee of Bordeaux examined and validated our protocol (N° 330110002-A). Neurons were transfected using Effectene (Qiagen) at 7 days *in vitro* (DIV) for spines and for filopodia experiments. For experiments performed on growth cones, neurons were transfected by nucleofection at the time of plating (Nucleofector™ II Device, Lonza Cologne GmBH, Germany). Experiments were performed at 17–21 DIV for mature dendritic spines, 9–11 DIV for dendritic filopodia and 3–4 DIV for growth cones. mEOS2-Abi1, mEOS2-Nap1, mEOS2-ArpC5A, mEOS2-CAAX, mEOS2-IRSp53, mEOS2-Rac1, mEOS2-Rac1-Q61L, mEOS2-Rac1-T17N and mEOS2-VASP were generated by PCR of the coding DNA sequence of the corresponding protein and inserted in the pcDNAm-FRT-PC-mESO2 blue at the FseI/AscI site. GFP-ArpC5A and GFP-Abi1 were generated by PCR of the coding DNA sequence of the corresponding protein and inserted in the pcDNAm-FRT-PC-GFP blue at the FseI/AscI site. The human FMNL2-mEOS2 construct was generated by replacing the GFP of the FMNL2-GFP (pEGFP-N1) (Block *et al*, 2012) by mEOS2 at the AgeI/NotI sites, and mEOS2 fragment was obtained by PCR on PrSet-A mEOS2 (Addgene). Cerulean-Rac1-Q61L was generated by PCR of Rac1-Q61L, which was inserted in pEGFP-C1 (Clonetech) at the BglII/KpnI sites, and then GFP was replaced by cerulean at NheI/BglII sites. Actin-mEOS2 construct was generated as described before (Rossier *et al*, 2012). mEOS2-PSD-95 and Homer-1c-DsRed were, respectively, subcloned from PSD95-EGFP and Homer1c:GFP as described previously (Mondin *et al*, 2011). GFP-VASP (Rottner *et al*, 1999) was provided by Juergen Wehland (German Research Center for Biotechnology, Germany). Shank3-GFP was a gift from Nathalie Sans (Neurocentre Magendie, Bordeaux, France). The fidelity of all constructs was verified by sequencing.

Immunostaining

Neurons transfected with the appropriate construct were fixed for 10 min in warm 4% paraformaldehyde and 4% sucrose in PBS. Remaining active sites were saturated with 50 mM NH_4Cl in PBS for 15 min. For intracellular labeling, neurons were permeabilized 5 min with 0.1% of Triton X-100 (Sigma-Aldrich), washed with PBS and incubated with PBS containing 1% BSA for 30 min. For endogenous labeling of PSD95, neurons were incubated with mouse anti-PSD95 antibody (MA1-046, Thermo Fisher Scientific, USA, used at 2 μg ml^{-1}) for 30 min at room temperature and washed with PBS containing 1% BSA. For endogenous labeling of actin regulators, neurons were incubated over night at 4°C and washed with PBS containing 1% BSA. Antibodies used for those immunostainings are ArpC5 (Synaptic System, 323H3), FMNL2 (abcam, ab57963), WAVE1 (NeuroMab; 75-048) and WAVE2 kindly provided by Giorgio Scita (IFOM, Fondazione Istituto FIRC di Oncologia Molecolare, Milan, Italy) and polyclonal VASP kindly provided by Theresia Stradal (Helmholtz Centre for Infection Research, Braunschweig, Germany) (Jenzora *et al*, 2005). The primary antibodies were then revealed by incubating Alexa647-coupled anti-mouse or anti-rabbit IgG secondary antibody (Invitrogen, donkey, used at 1 μg ml^{-1}) for 30 min/1 h at room temperature.

sptPALM acquisitions

Neurons were imaged at 37°C in a Ludin chamber (Life Imaging Services) with an inverted motorized microscope (Nikon Ti) equipped with a 100x1.45 NA PL-APO objective and a perfect focus system, allowing long acquisition in oblique illumination mode. For photoactivation localization microscopy, neurons expressing mEOS2 tagged constructs were photoactivated using a 405 nm laser (Omicron) and the resulting photoconverted single-molecule fluorescence was excited with a 561 nm laser (Cobolt Jive™). Both lasers illuminated the sample simultaneously. Their respective power was adjusted to keep the number of the stochastically activated

molecules constant and well separated during the acquisition. Fluorescence was collected by the combination of dichroic and emission filters (F38-561 and F39-617 respectively, Semrock, Rochester, USA) and a sensitive EMCCD camera (Evolve, Photometrics). The acquisition was steered by MetaMorph software (Molecular Devices). Trajectory analyses of proteins fused to mEOS2 were performed at 20 Hz streaming acquisitions, with 561 nm low-power laser illumination (3–4 kw cm^{-2}) (Figs 4–6 and Supplementary Figs S5, S6, S8 and S9). For high-frequency localization of mEOS2 fused proteins, we used 561 nm higher-power laser illumination (7–8 kw cm^{-2}) and 100 Hz streaming acquisition (Fig 2 and Supplementary Figs S1A, S2 and S3). Quantification of actin-mEOS2 and mEOS2-ArpC5A flow were performed at low-frequency acquisition (2 Hz) with long-exposure time (250 ms) and low power 561 nm laser illumination (1.5 kw cm^{-2}) to only capture mEOS2 slow movements (Fig 1). To test the phototoxicity of sptPALM acquisitions, we verified that spine motility was preserved at the end of experiments. Diffraction-limited fluorescence images of mEOS2 and GFP constructs were imaged using a conventional GFP filter cube (ET470/40, T495LPXR, ET525/50, Chroma). We used multicolor fluorescent 100-nm beads (Tetraspeck, Invitrogen) as fiducial markers to register long-term acquisitions and correct for lateral drifts.

Single-molecule localization and tracking

sptPALM experiments lead to sets of 8,000–20,000 images per cell, analyzed by dedicated custom-made image analysis software in order to extract molecule localization and dynamics. Fluorescent single molecules were localized and tracked over time using a combination of wavelet segmentation and simulated annealing algorithms (Racine *et al*, 2006, 2007; Izeddin *et al*, 2012; Rossier *et al*, 2012; Kechkar *et al*, 2013) operating as a plug-in inside MetaMorph software (Molecular Devices). Under the experimental conditions described above, the resolution of the system was quantified to ~55 nm (full width at half maximum, FWHM). This spatial resolution depends on the molecule's signal to noise ratio and the segmentation algorithm (Cheezum *et al*, 2001) and was determined using fixed mEOS2 samples. We analyzed hundreds of two-dimensional distributions of single-molecule positions belonging to long trajectories (> 30 frames) by bi-dimensional Gaussian fitting, the resolution being determined as $2.3\sigma_{xy}$, where σ_{xy} is the pointing accuracy. For the trajectory analysis, spines and shafts were identified manually in the corresponding super-resolution intensity images. The corresponding regions of interest were used to sort single particle data analyses to specific regions.

We analyzed trajectories lasting at least 13 points (> 650 ms) with a custom routine (Matlab, Matworks) using the mean-squared displacement (*MSD*) computed as (equation 1):

$$MSD(t = n \cdot \Delta t) = \frac{\sum_{i=1}^{N-n} (x_{i+n} - x_i)^2 + (y_{i+n} - y_i)^2}{N - n} \quad (1)$$

where x_i and y_i are the coordinates of the label position at time $i{\cdot}\Delta t$. We defined the measured diffusion coefficient D as the slope of the affine regression line fitted to the $n = 1$–4 values of the *MSD* ($n{\cdot}\Delta t$). The *MSD* was computed and then fitted on a duration equal to 80% (minimum of 10 points, 500 ms) of the whole stretch by (equation 2):

$$MSD(t) = \frac{4r_{conf}^2}{3}(1 - e^{-t/\tau}) \quad (2)$$

where r_{conf} is the measured confinement radius and τ the time constant ($\tau = r_{conf}^2/3D_{conf}$). To reduce the inaccuracy of the MSD fit due to down sampling for larger time intervals, we used a weighted fit. Trajectories were sorted in three groups: immobile, confined diffusion and free-diffusion. Immobile trajectories were defined as trajectories with $D < 0.004\ \mu m^2\ s^{-1}$, corresponding to molecules that explored an area inferior to the one defined by the image spatial resolution ~$(0.055\ \mu m)^2$ during the time used to fit the initial slope of the MSD (Rossier *et al*, 2012) (four points, 80 ms):

$$D_{threshold} = (0.055\ \mu m)^2/(4 \times 4 \times 0.05\ s) \sim 0.004\ \mu m^2\ s^{-1}$$

To separate trajectories displaying free-diffusion from confined diffusion, we used the time constant τ calculated for each trajectory. Confined and free-diffusing trajectories were defined as trajectories with a time constant τ, respectively, inferior and superior to half the time interval used to compute the MSD (250 ms).

Note that with the acquisition frequency and oblique illumination used in our experiments, it is impossible to reconnect trajectories lasting at least 650 ms (> 13 points) for a protein freely diffusing in 3D within the cytosol. In the case of a mEOS2 alone, trajectories that can be reconstructed correspond mainly to a low fraction of mEOS2 non-specifically interacting with membrane components. Therefore, counter intuitively, a mEOS2 alone freely diffusing in the cytosol will result in a distribution of D further shifted toward slower D compared to a protein freely diffusing on the membrane: compare Fig 4G–I (cyto, purple) and Fig 5G–I (CAAX, magenta).

For flow measurements of actin-mEOS2 and mEOS2-ArpC5A in spines, filopodia and growth cones, localization and tracking were performed as described above for streaming acquisition. We analyzed trajectories longer than eight points (4 s), giving a minimal resolution of 6 nm s^{-1} (55 nm/2.3/4 s). A custom routine (Matlab, Matworks) calculated the start to end distance (nm), the duration (sec) and the corresponding speed (nm s^{-1}) of trajectories.

Dual-color sequential dSTORM/PALM

Fixed and stained neurons were imaged at room temperature in a closed Ludin chamber (Life Imaging Services) mounted on an inverted motorized microscope (Nikon Ti) equipped with a 100x1.45NA PL-APO objective and a perfect focus system, allowing long acquisition in oblique illumination mode. Imaging was performed in a solution (water, glucose, glycerol) containing reducing (aliphatic thiols) and oxygen scavengers (glucose oxydase). For dSTORM, ensemble fluorescence of Alexa647 was first converted into dark state using a 640 nm laser at 30–50 kw cm^{-2} intensity. Once the ensemble fluorescence converted into the desired density of single molecules per image, the laser power was reduced to 7–15 kw cm^{-2} and streaming acquisition was performed at 50–100 Hz for 20,000 frames. The density of single molecules per frame was controlled by using a 405 nm laser (Omicron, Germany). The laser powers were adjusted to keep a specific optimal level of stochastically activated molecules which were well separated during the acquisition using an automatic feedback control (Kechkar *et al*, 2013).

PALM streaming sequences of the mEOS2 construct (50–100 Hz for 20,000 frames) was performed right after the dSTORM sequence using a 561 nm laser at 7–15 kw cm^{-2}. Both the ensemble and single-molecule fluorescence were collected by the combination of dichroic (F73-866 (Alexa647) and F38-561 (mEOS2), Semrock) and emission filter (F37-692 (Alexa647) and F39-617 (mEOS2), Semrock). The fluorescence was collected using a sensitive EMCCD camera (Evolve, Photometric). The acquisition sequence was driven by MetaMorph software (Molecular Devices). We used multicolor fluorescent microbeads (Tetraspeck, Invitrogen) as fiducial markers to register long-term acquisitions and correct for lateral drifts and chromatic shifts. Single-molecule localization and super-resolution image generation were performed as described in the single-molecule localization method section.

Dispersion analysis

We first generated sptPALM acquisitions using fast acquisition frequency (100 Hz; 8,000–12,000 frames; 80–120 s). Fluorescent single molecules were localized as described above. We generated a super-resolution time-lapse sequence (frame rate 5 s, 500 images) from which high-density zones of localizations were identified using wavelet-based segmentation method (Racine *et al*, 2006, 2007; Izeddin *et al*, 2012; Rossier *et al*, 2012; Kechkar *et al*, 2013). High-density zones correspond to locations where repetitive mEOS2 fluorescence was detected. This analysis allowed to reject fast diffusing molecules and to select specifically zones of immobilized or slowly mobile molecules. For each spine, we quantified the distances of each zone compared to the centroid of all detected zones. For each condition, we used box plots displaying the median and mean of distance distribution from the centroid of all zones (Supplementary Fig S3D). Dual-color PALM/dSTORM experiments were analyzed similarly, except that we measured the distances between mEOS2 high-density zones with respect to the centroid of PSD-95-A647 zones (Figs 3E and 7C, and Supplementary Fig S6C).

Domain size analysis

ArpC5A, Abi1, VASP, IRSp53 and PSD95 domains were identified from super-resolution images by custom software written as a plug-in running inside MetaMorph software. Single-molecule-based super-resolution images were reconstructed from the 20,000 frames before being analyzed. Domains, which corresponded to clusters of high-density zones, were first identified by wavelet segmentation. Domain dimensions were then computed by two-dimensional anisotropic Gaussian fitting, from which the long and the short axes were extracted as $2.3\sigma_{long}$ and $2.3\sigma_{short}$, respectively. The long and the short axes of each domain were exported to calculate their respective distribution, median and mean (Fig 3D and Supplementary Fig S6B).

Statistical analysis

D'Agostino and Pearson omnibus test was used to test whether values in each sample came from a Gaussian distribution (normality test). Non-Gaussian distributions of speeds (Fig 1D), distances (Figs 3E and 7C, and Supplementary S6C), domain sizes (Fig 3D and Supplementary Fig S6B) and diffusion coefficient (Figs 4I, 5I and 6I) were represented by box plots displaying the median (notch) and mean (square) ± percentile (25–75%) and compared two by two using non-parametric, two-tailed Mann–Whitney rank sum test. Small samples, such as fractions of immobilization (Figs 4H, 5H and 6H), were represented as mean ± SEM and compared using two-tailed unpaired *t*-test.

Supplementary information for this article is available online: http://emboj.embopress.org

Acknowledgements

We thank B. Tessier, F. Neca, C. Breillat, A. Frouin, D. Bouchet, P. Gonzales and R. Sterling for technical assistance; M. Garcia, J. Petersen, O. Rossier, M. Mondin and N. Sans for helpful discussions; O. Rossier and L. Blanchoin for critical reading of the manuscript; and M. Mondin, P. Legros and C. Poujol of the Bordeaux Imaging Center. We thank N. Sans for providing Shank3-GFP construct, Giorgio Scita for the WAVE-2 antibody and Theresia Stradal for the VASP antibody. We acknowledge financial support from the French Ministry of Research and CNRS, ANR grant Nanomotility (GG), LabEx BRAIN, Conseil Régional Aquitaine, Fondation pour la Recherche Médicale, the ERC Program no. 232942 Nano-Dyn-Syn (DC) and no. 235552 Glutraf (DN) and the Deutsche Forschungsgemeinschaft (KR).

Author contributions

GG conceived and coordinated the study. AC and GG conceptualized the experiments. AC performed most of the experiments. AM performed the experiments on Nap1 and endogenous WAVE. AC, AM and IC performed control chemical LTP experiments. JG, FK, KR and AG designed and generated new protein constructs. DN, AK and JBS developed the sptPALM and dSTORM setup. AK and JBS developed the analytical tools for sptPALM, PALM and dSTORM. CL developed the analytical tools in Matlab used for single protein tracking, flow measurement and representation. AC, AM and GG analyzed the data. JBS, AG, KR, DC and OT contributed scientifically. AC and GG wrote the manuscript and supplement. All authors discussed the results and commented on the manuscript.

Conflict of interest

The authors declare that they have no conflict of interest.

References

Achard V, Martiel J-LL, Michelot A, Guérin C, Reymann A-CC, Blanchoin L, Boujemaa-Paterski R, Guerin C (2010) A "primer"-based mechanism underlies branched actin filament network formation and motility. *Curr Biol* 20: 423 – 428

Ackermann M, Matus A (2003) Activity-induced targeting of profilin and stabilization of dendritic spine morphology. *Nat Neurosci* 6: 1194 – 1200

Bats C, Groc L, Choquet D (2007) The interaction between Stargazin and PSD-95 regulates AMPA receptor surface trafficking. *Neuron* 53: 719 – 734

Bear JE, Svitkina TM, Krause M, Schafer DA, Loureiro JJ, Strasser GA, Maly IV, Chaga OY, Cooper JA, Borisy GG, Gertler FB (2002) Antagonism between Ena/VASP proteins and actin filament capping regulates fibroblast motility. *Cell* 109: 509 – 521

Berning S, Willig KI, Steffens H, Dibaj P, Hell SW (2012) Nanoscopy in a living mouse brain. *Science* 335: 551

Betzig E, Patterson GH, Sougrat R, Lindwasser OW, Olenych S, Bonifacino JS, Davidson MW, Lippincott-Schwartz J, Hess HF (2006) Imaging intracellular fluorescent proteins at nanometer resolution. *Science* 313: 1642 – 1645

Block J, Breitsprecher D, Kühn S, Winterhoff M, Kage F, Geffers R, Duwe P, Rohn JL, Baum B, Brakebusch C, Kuhn S, Geyer M, Stradal TEB, Faix J, Rottner K (2012) FMNL2 drives actin-based protrusion and migration downstream of Cdc42. *Curr Biol* 22: 1005 – 1012

Bockmann J, Kreutz MR, Gundelfinger ED, Bockers TM (2002) ProSAP/Shank postsynaptic density proteins interact with insulin receptor tyrosine kinase substrate IRSp53. *J Neurochem* 83: 1013 – 1017

Bosch M, Castro J, Saneyoshi T, Matsuno H, Sur M, Hayashi Y (2014) Structural and molecular remodeling of dendritic spine substructures during long-term potentiation. *Neuron* 82: 444 – 459

Breitsprecher D, Kiesewetter AK, Linkner J, Vinzenz M, Stradal TEB, Small JV, Curth U, Dickinson RB, Faix J (2011) Molecular mechanism of Ena/VASP-mediated actin-filament elongation. *EMBO J* 30: 456 – 467

Charrier C, Joshi K, Coutinho-Budd J, Kim J-E, Lambert N, de Marchena J, Jin W-L, Vanderhaeghen P, Ghosh A, Sassa T, Polleux F (2012) Inhibition of SRGAP2 function by its human-specific paralogs induces neoteny during spine maturation. *Cell* 149: 923 – 935

Cheezum MK, Walker WF, Guilford WH (2001) Quantitative comparison of algorithms for tracking single fluorescent particles. *Biophys J* 81: 2378 – 2388

Chen Z, Borek D, Padrick SB, Gomez TS, Metlagel Z, Ismail AM, Umetani J, Billadeau DD, Otwinowski Z, Rosen MK (2010) Structure and control of the actin regulatory WAVE complex. *Nature* 468: 533 – 538

Chen B, Brinkmann K, Chen Z, Pak CW, Liao Y, Shi S, Henry L, Grishin NV, Bogdan S, Rosen MK (2014) The WAVE regulatory complex links diverse receptors to the actin cytoskeleton. *Cell* 156: 195 – 207

Choi J, Ko J, Racz B, Burette A, Lee J-RR, Kim S, Na M, Lee HW, Kim K, Weinberg RJ, Kim E (2005) Regulation of dendritic spine morphogenesis by insulin receptor substrate 53, a downstream effector of Rac1 and Cdc42 small GTPases. *J Neurosci* 25: 869 – 879

Cingolani LA, Goda Y (2008) Actin in action: the interplay between the actin cytoskeleton and synaptic efficacy. *Nat Rev Neurosci* 9: 344 – 356

Craven SE, El-Husseini AE, Bredt DS (1999) Synaptic targeting of the postsynaptic density protein PSD-95 mediated by lipid and protein motifs. *Neuron* 22: 497 – 509

Dani A, Huang B, Bergan J, Dulac C, Zhuang X (2010) Superresolution imaging of chemical synapses in the brain. *Neuron* 68: 843 – 856

De Rubeis S, Pasciuto E, Li KW, Fernández E, Di Marino D, Buzzi A, Ostroff LE, Klann E, Zwartkruis FJT, Komiyama NH, Grant SGN, Poujol C, Choquet D, Achsel T, Posthuma D, Smit AB, Bagni C (2013) CYFIP1 coordinates mRNA translation and cytoskeleton remodeling to ensure proper dendritic spine formation. *Neuron* 79: 1169 – 1182

Dunaevsky A, Tashiro A, Majewska A, Mason C, Yuste R (1999) Developmental regulation of spine motility in the mammalian central nervous system. *Proc Natl Acad Sci U S A* 96: 13438 – 13443

Durand CM, Perroy J, Loll F, Perrais D, Fagni L, Bourgeron T, Montcouquiol M, Sans N (2012) SHANK3 mutations identified in autism lead to modification of dendritic spine morphology via an actin-dependent mechanism. *Mol Psychiatry* 17: 71 – 84

Edwards FA (1998) Dancing dendrites. *Nature* 394: 129 – 130

Fan Y, Tang X, Vitriol E, Chen G, Zheng JQ (2011) Actin capping protein is required for dendritic spine development and synapse formation. *J Neurosci* 31: 10228 – 10233

Fifkova E, Delay RJ (1982) Cytoplasmic actin in neuronal processes as a possible mediator of synaptic plasticity. *J Cell Biol* 95: 345 – 350

Fischer M, Kaech S, Knutti D, Matus A (1998) Rapid actin-based plasticity in dendritic spines. *Neuron* 20: 847 – 854

Fortin DA, Davare MA, Srivastava T, Brady JD, Nygaard S, Derkach VA, Soderling TR (2010) Long-term potentiation-dependent spine enlargement requires synaptic Ca2+-permeable AMPA receptors recruited by CaM-kinase I. *J Neurosci* 30: 11565 – 11575

Frost NA, Shroff H, Kong H, Betzig E, Blanpied TA (2010) Single-molecule discrimination of discrete perisynaptic and distributed sites of actin filament assembly within dendritic spines. *Neuron* 67: 86 – 99

Fukata Y, Dimitrov A, Boncompain G, Vielemeyer O, Perez F, Fukata M (2013) Local palmitoylation cycles define activity-regulated postsynaptic subdomains. *J Cell Biol* 202: 145 – 161

Gardberg M, Talvinen K, Kaipio K, Iljin K, Kampf C, Uhlen M, Carpén O (2010) Characterization of Diaphanous-related formin FMNL2 in human tissues. *BMC Cell Biol* 11: 55

Gautreau A, Ho HYHY, Li J, Steen H, Gygi SP, Kirschner MW (2004) Purification and architecture of the ubiquitous Wave complex. *Proc Natl Acad Sci U S A* 101: 4379 – 4383

Giannone G, Dubin-Thaler BJ, Döbereiner H-G, Kieffer N, Bresnick AR, Sheetz MP (2004) Periodic lamellipodial contractions correlate with rearward actin waves. *Cell* 116: 431 – 443

Giannone G, Dubin-Thaler BJ, Rossier O, Cai Y, Chaga O, Jiang G, Beaver W, Döbereiner H-G, Freund Y, Borisy G, Sheetz MP (2007) Lamellipodial actin mechanically links myosin activity with adhesion-site formation. *Cell* 128: 561 – 575

Govek E-E, Newey SE, Van Aelst L (2005) The role of the Rho GTPases in neuronal development. *Genes Dev* 19: 1 – 49

Gu J, Lee CW, Fan Y, Komlos D, Tang X, Sun C, Yu K, Hartzell HC, Chen G, Bamburg JR, Zheng JQ (2010) ADF/cofilin-mediated actin dynamics regulate AMPA receptor trafficking during synaptic plasticity. *Nat Neurosci* 13: 1208 – 1215

Haditsch U, Leone DP, Farinelli M, Chrostek-Grashoff A, Brakebusch C, Mansuy IM, McConnell SK, Palmer TD (2009) A central role for the small GTPase Rac1 in hippocampal plasticity and spatial learning and memory. *Mol Cell Neurosci* 41: 409 – 419

Han K, Holder JL, Schaaf CP, Lu H, Chen H, Kang H, Tang J, Wu Z, Hao S, Cheung SW, Yu P, Sun H, Breman AM, Patel A, Lu H-C, Zoghbi HY (2013) SHANK3 overexpression causes manic-like behaviour with unique pharmacogenetic properties. *Nature* 503: 72 – 77

Hering H, Sheng M (2003) Activity-dependent redistribution and essential role of cortactin in dendritic spine morphogenesis. *J Neurosci* 23: 11759 – 11769

Honkura N, Matsuzaki M, Noguchi J, Ellis-Davies GCR, Kasai H (2008) The subspine organization of actin fibers regulates the structure and plasticity of dendritic spines. *Neuron* 57: 719 – 729

Hotulainen P, Llano O, Smirnov S, Tanhuanpaa K, Faix J, Rivera C, Lappalainen P, Tanhuanpää K (2009) Defining mechanisms of actin polymerization and depolymerization during dendritic spine morphogenesis. *J Cell Biol* 185: 323 – 339

Hotulainen P, Hoogenraad CC (2010) Actin in dendritic spines: connecting dynamics to function. *J Cell Biol* 189: 619 – 629

Innocenti M, Zucconi A, Disanza A, Frittoli E, Areces LB, Steffen A, Stradal TEB, Di Fiore PP, Carlier M-F, Scita G (2004) Abi1 is essential for the formation and activation of a WAVE2 signalling complex. *Nat Cell Biol* 6: 319 – 327

Iwasa JH, Mullins RD (2007) Spatial and temporal relationships between actin-filament nucleation, capping, and disassembly. *Curr Biol* 17: 395 – 406

Izeddin I, Specht CG, Lelek M, Darzacq X, Triller A, Zimmer C, Dahan M (2011) Super-resolution dynamic imaging of dendritic spines using a low-affinity photoconvertible actin probe. *PLoS ONE* 6: e15611

Izeddin I, Boulanger J, Racine V, Specht CG, Kechkar A, Nair D, Triller A, Choquet D, Dahan M, Sibarita JB (2012) Wavelet analysis for single molecule localization microscopy. *Opt Express* 20: 2081 – 2095

Jenzora A, Behrendt B, Small JV, Wehland J, Stradal TEB (2005) PREL1 provides a link from Ras signalling to the actin cytoskeleton via Ena/VASP proteins. *FEBS Lett* 579: 455 – 463

Kechkar A, Nair D, Heilemann M, Choquet D, Sibarita J-B (2013) Real-time analysis and visualization for single-molecule based super-resolution microscopy. *PLoS ONE* 8: e62918

Kim Y, Sung JY, Ceglia I, Lee K-W, Ahn J-H, Halford JM, Kim AM, Kwak SP, Park JB, Ho Ryu S, Schenck A, Bardoni B, Scott JD, Nairn AC, Greengard P (2006) Phosphorylation of WAVE1 regulates actin polymerization and dendritic spine morphology. *Nature* 442: 814 – 817

Kim IH, Racz B, Wang H, Burianek L, Weinberg R, Yasuda R, Wetsel WC, Soderling SH (2013) Disruption of Arp2/3 results in asymmetric structural plasticity of dendritic spines and progressive synaptic and behavioral abnormalities. *J Neurosci* 33: 6081 – 6092

Korobova F, Svitkina T (2010) Molecular architecture of synaptic actin cytoskeleton in hippocampal neurons reveals a mechanism of dendritic spine morphogenesis. *Mol Biol Cell* 21: 165 – 176

Koronakis V, Hume PJ, Humphreys D, Liu T, Hørning O, Jensen ON, McGhie EJ (2011) WAVE regulatory complex activation by cooperating GTPases Arf and Rac1. *Proc Natl Acad Sci U S A* 108: 14449 – 14454

Lai FPL, Szczodrak M, Block J, Faix J, Breitsprecher D, Mannherz HG, Stradal TEB, Dunn GA, Small JV, Rottner K (2008) Arp2/3 complex interactions and actin network turnover in lamellipodia. *EMBO J* 27: 982 – 992

Lanier LM, Gates MA, Witke W, Menzies AS, Wehman AM, Macklis JD, Kwiatkowski D, Soriano P, Gertler FB (1999) Mena is required for neurulation and commissure formation. *Neuron* 22: 313 – 325

Lebensohn AM, Kirschner MW (2009) Activation of the WAVE complex by coincident signals controls actin assembly. *Mol Cell* 36: 512 – 524

Lendvai B, Stern EA, Chen B, Svoboda K (2000) Experience-dependent plasticity of dendritic spines in the developing rat barrel cortex in vivo. *Nature* 404: 876 – 881

Lin Y-C, Redmond L (2008) CaMKIIbeta binding to stable F-actin in vivo regulates F-actin filament stability. *Proc Natl Acad Sci U S A* 105: 15791 – 15796

Lin WH, Nebhan CA, Anderson BR, Webb DJ (2010) Vasodilator-stimulated phosphoprotein (VASP) induces actin assembly in dendritic spines to promote their development and potentiate synaptic strength. *J Biol Chem* 285: 36010 – 36020

Lippi G, Steinert JR, Marczylo EL, D'Oro S, Fiore R, Forsythe ID, Schratt G, Zoli M, Nicotera P, Young KW (2011) Targeting of the Arpc3 actin nucleation factor by miR-29a/b regulates dendritic spine morphology. *J Cell Biol* 194: 889 – 904

MacGillavry HD, Song Y, Raghavachari S, Blanpied TA (2013) Nanoscale scaffolding domains within the postsynaptic density concentrate synaptic AMPA receptors. *Neuron* 78: 615 – 622

Maglione M, Sigrist SJ (2013) Seeing the forest tree by tree: super-resolution light microscopy meets the neurosciences. *Nat Neurosci* 16: 790 – 797

Manley S, Gillette JM, Patterson GH, Shroff H, Hess HF, Betzig E, Lippincott-Schwartz J (2008) High-density mapping of single-molecule trajectories with photoactivated localization microscopy. *Nat Methods* 5: 155

Matsuzaki M, Honkura N, Ellis-Davies GC, Kasai H (2004) Structural basis of long-term potentiation in single dendritic spines. *Nature* 429: 761 – 766

Medeiros NA, Burnette DT, Forscher P (2006) Myosin II functions in actin-bundle turnover in neuronal growth cones. *Nat Cell Biol* 8: 215 – 226

Miki H, Yamaguchi H, Suetsugu S, Takenawa T (2000) IRSp53 is an essential intermediate between Rac and WAVE in the regulation of membrane ruffling. *Nature* 408: 732 – 735

Millius A, Watanabe N, Weiner OD (2012) Diffusion, capture and recycling of SCAR/WAVE and Arp2/3 complexes observed in cells by single-molecule imaging. *J Cell Sci* 125: 1165 – 1176

Mondin M, Labrousse V, Hosy E, Heine M, Tessier B, Levet F, Poujol C, Blanchet C, Choquet D, Thoumine O (2011) Neurexin-neuroligin adhesions capture surface-diffusing AMPA receptors through PSD-95 scaffolds. *J Neurosci* 31: 13500 – 13515

Murakoshi H, Wang H, Yasuda R (2011) Local, persistent activation of Rho GTPases during plasticity of single dendritic spines. *Nature* 472: 100 – 104

Nair D, Hosy E, Petersen JD, Constals A, Giannone G, Choquet D, Sibarita J-B (2013) Super-resolution imaging reveals that AMPA receptors inside synapses are dynamically organized in nanodomains regulated by PSD95. *J Neurosci* 33: 13204 – 13224

Nakagawa H, Miki H, Nozumi M, Takenawa T, Miyamoto S, Wehland J, Small JV (2003) IRSp53 is colocalised with WAVE2 at the tips of protruding lamellipodia and filopodia independently of Mena. *J Cell Sci* 116: 2577 – 2583

Okamoto K, Nagai T, Miyawaki A, Hayashi Y (2004) Rapid and persistent modulation of actin dynamics regulates postsynaptic reorganization underlying bidirectional plasticity. *Nat Neurosci* 7: 1104 – 1112

Okamoto K-I, Narayanan R, Lee SH, Murata K, Hayashi Y (2007) The role of CaMKII as an F-actin-bundling protein crucial for maintenance of dendritic spine structure. *Proc Natl Acad Sci U S A* 104: 6418 – 6423

Okamoto K, Bosch M, Hayashi Y (2009) The roles of CaMKII and F-actin in the structural plasticity of dendritic spines: a potential molecular identity of a synaptic tag? *Physiology* 24: 357 – 366

Padrick SB, Rosen MK (2010) Physical mechanisms of signal integration by WASP family proteins. *Annu Rev Biochem* 79: 707 – 735

Park E, Chi S, Park D (2012) Activity-dependent modulation of the interaction between CaMKIIα and Abi1 and its involvement in spine maturation. *J Neurosci* 32: 13177 – 13188

Penzes P, Cahill ME, Jones KA, VanLeeuwen J-E, Woolfrey KM (2011) Dendritic spine pathology in neuropsychiatric disorders. *Nat Neurosci* 14: 285 – 293

Pollard TD, Cooper JA (2009) Actin, a central player in cell shape and movement. *Science* 326: 1208 – 1212

Ponti A, Machacek M, Gupton SL, Waterman-Storer CM, Danuser G (2004) Two distinct actin networks drive the protrusion of migrating cells. *Science* 305: 1782 – 1786

Proepper C, Johannsen S, Liebau S, Dahl J, Vaida B, Bockmann J, Kreutz MR, Gundelfinger ED, Boeckers TM (2007) Abelson interacting protein 1 (Abi-1) is essential for dendrite morphogenesis and synapse formation. *EMBO J* 26: 1397 – 1409

Racine V, Hertzog A, Jouanneau J, Salamero J, Kervrann C, Sibarita JB (2006) Multiple-target tracking of 3D fluorescent objects based on simulated annealing. *3rd IEEE Int Symp Biomed Imaging*. 1020 – 1023

Racine V, Sachse M, Salamero J, Fraisier V, Trubuil A, Sibarita JB (2007) Visualization and quantification of vesicle trafficking on a three-dimensional cytoskeleton network in living cells. *J Microsc* 225: 214 – 228

Rácz B, Weinberg RJ, Racz B (2013) Microdomains in forebrain spines: an ultrastructural perspective. *Mol Neurobiol* 47: 77 – 89

Rossier O, Octeau V, Sibarita J-BB, Leduc C, Tessier B, Nair D, Gatterdam V, Destaing O, Albiges-Rizo C, Tampe R, Cognet L, Choquet D, Lounis B, Giannone G (2012) Integrins beta(1) and beta(3) exhibit distinct dynamic nanoscale organizations inside focal adhesions. *Nat Cell Biol* 14: 1057 – 1067

Rottner K, Behrendt B, Small JV, Wehland J (1999) VASP dynamics during lamellipodia protrusion. *Nat Cell Biol* 1: 321 – 322

Rust MB, Gurniak CB, Renner M, Vara H, Morando L, Görlich A, Sassoè-Pognetto M, Banchaabouchi MA, Giustetto M, Triller A, Choquet D, Witke W (2010) Learning, AMPA receptor mobility and synaptic plasticity depend on n-cofilin-mediated actin dynamics. *EMBO J* 29: 1889 – 1902

Sala C, Piëch V, Wilson NR, Passafaro M, Liu G, Sheng M (2001) Regulation of dendritic spine morphology and synaptic function by Shank and Homer. *Neuron* 31: 115 – 130

Schenck A, Bardoni B, Langmann C, Harden N, Mandel JL, Giangrande A (2003) CYFIP/Sra-1 controls neuronal connectivity in *Drosophila* and links the Rac1 GTPase pathway to the fragile X protein. *Neuron* 38: 887 – 898

Scita G, Confalonieri S, Lappalainen P, Suetsugu S (2008) IRSp53: crossing the road of membrane and actin dynamics in the formation of membrane protrusions. *Trends Cell Biol* 18: 52 – 60

Sheng M, Hoogenraad CC (2007) The postsynaptic architecture of excitatory synapses: a more quantitative view. *Annu Rev Biochem* 76: 823 – 847

Shibata ACE, Chen LH, Nagai R, Ishidate F, Chadda R, Miwa Y, Naruse K, Shirai YM, Fujiwara TK, Kusumi A (2013) Rac1 recruitment to the archipelago structure of the focal adhesion through the fluid membrane as revealed by single-molecule analysis. *Cytoskeleton (Hoboken)* 177: 161 – 177

Shroff H, Galbraith CG, Galbraith JA, Betzig E (2008) Live-cell photoactivated localization microscopy of nanoscale adhesion dynamics. *Nat Methods* 5: 417 – 423

Soderling SH, Langeberg LK, Soderling JA, Davee SM, Simerly R, Raber J, Scott JD (2003) Loss of WAVE-1 causes sensorimotor retardation and reduced learning and memory in mice. *Proc Natl Acad Sci U S A* 100: 1723 – 1728

Soderling SH, Guire ES, Kaech S, White J, Zhang F, Schutz K, Langeberg LK, Banker G, Raber J, Scott JD (2007) A WAVE-1 and WRP signaling complex regulates spine density, synaptic plasticity, and memory. *J Neurosci* 27: 355 – 365

Spacek J, Harris KM (2004) Trans-endocytosis via spinules in adult rat hippocampus. *J Neurosci* 24: 4233 – 4241

Star EN, Kwiatkowski DJ, Murthy VN (2002) Rapid turnover of actin in dendritic spines and its regulation by activity. *Nat Neurosci* 5: 239 – 246

Steffen A, Rottner K, Ehinger J, Innocenti M, Scita G, Wehland J, Stradal TEB (2004) Sra-1 and Nap1 link Rac to actin assembly driving lamellipodia formation. *EMBO J* 23: 749 – 759

Sturgill JF, Steiner P, Czervionke BL, Sabatini BL (2009) Distinct domains within PSD-95 mediate synaptic incorporation, stabilization, and activity-dependent trafficking. *J Neurosci* 29: 12845 – 12854

Suetsugu S, Kurisu S, Oikawa T, Yamazaki D, Oda A, Takenawa T (2006) Optimization of WAVE2 complex-induced actin polymerization by membrane-bound IRSp53, PIP(3), and Rac. *J Cell Biol* 173: 571 – 585

Svitkina TM, Bulanova EA, Chaga OY, Vignjevic DM, Kojima S, Vasiliev JM, Borisy GG (2003) Mechanism of filopodia initiation by reorganization of a dendritic network. *J Cell Biol* 160: 409 – 421

Tashiro A, Yuste R (2004) Regulation of dendritic spine motility and stability by Rac1 and Rho kinase: evidence for two forms of spine motility. *Mol Cell Neurosci* 26: 429 – 440

Tatavarty V, Kim E-J, Rodionov V, Yu J (2009) Investigating sub-spine actin dynamics in rat hippocampal neurons with super-resolution optical imaging. *PLoS ONE* 4: e7724

Tatavarty V, Das S, Yu J (2012) Polarization of actin cytoskeleton is reduced in dendritic protrusions during early spine development in hippocampal neuron. *Mol Biol Cell* 23: 3167 – 3177

Ueda Y, Hayashi Y (2013) PIP3 regulates spinule formation in dendritic spines during structural long-term potentiation. *J Neurosci* 33: 11040 – 11047

Van de Linde S, Loschberger A, Klein T, Heidbreder M, Wolter S, Heilemann M, Sauer M (2011) Direct stochastic optical reconstruction microscopy with standard fluorescent probes. *Nat Protoc* 6: 991 – 1009

Xie Z, Srivastava DP, Photowala H, Kai L, Cahill ME, Woolfrey KM, Shum CY, Surmeier DJ, Penzes P (2007) Kalirin-7 controls activity-dependent structural and functional plasticity of dendritic spines. *Neuron* 56: 640 – 656

Zhang Y, Matt L, Patriarchi T, Malik ZA, Chowdhury D, Park DK, Renieri A, Ames JB, Hell JW (2014) Capping of the N-terminus of PSD-95 by calmodulin triggers its postsynaptic release. *EMBO J* 33: 1 – 13

Zhou Q, Homma KJ, Poo MM (2004) Shrinkage of dendritic spines associated with long-term depression of hippocampal synapses. *Neuron* 44: 749 – 757

